

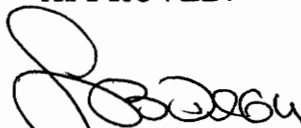
METALORGANIC CHEMICAL VAPOR DEPOSITION OF METAL OXIDES

by

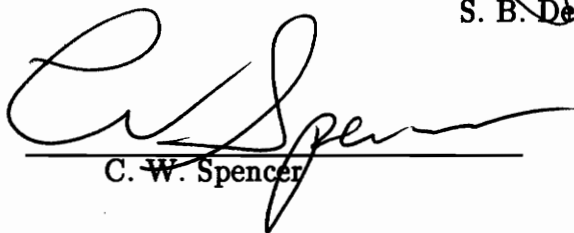
JIE SI

A thesis submitted to the faculty of
Virginia Polytechnic Institute and State University
in partial fulfillment of the requirements for the degree of
MASTER OF SCIENCE
in
Materials Science and Engineering

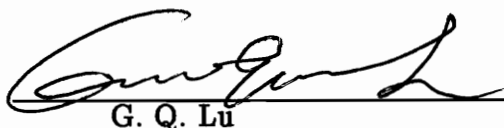
APPROVED:



S. B. Desu, Chairman



C. W. Spencer



G. Q. Lu

August, 1993
Blacksburg, Virginia

C.2

LD
5655
V855
1993
S56
C.2

METALORGANIC CHEMICAL VAPOR DEPOSITION OF METAL OXIDES

by

Jie Si

Committee Chairman: Seshu B. Desu

Materials Science and Engineering

(ABSTRACT)

Ruthenium dioxide, zirconium dioxide and bismuth titanate thin films were deposited on Si, sapphire disks, and Pt/Ti/SiO₂/Si substrates by hot wall metalorganic chemical vapor deposition (MOCVD). Bis(cyclopentadienyl)ruthenium [Ru(C₅H₅)₂], zirconium tetramethylheptanedione [Zr(thd)₄], triphenylbismuth [Bi(C₆H₅)₃], and titanium ethoxide [Ti(C₂H₅O)₄] were used as precursors.

MOCVD RuO₂ film structure was dependent on MOCVD process parameters such as bubbler temperature, dilute gas flow rates, deposition temperature, and total pressure. Either pure RuO₂, pure Ru, or a RuO₂ + Ru mixture was obtained under different deposition conditions. As-deposited pure RuO₂ films were specular, crack-free, and adhered well on the substrates. The Auger electron spectroscopy depth profile showed a good composition uniformity across the bulk of the films. The MOCVD RuO₂ thin films exhibited resistivities as low as 60 μΩ-cm. In addition, the reflectance of RuO₂ in the NIR region showed a metallic character.

Zr(thd)_4 was synthesized and the process was optimized. Purity of Zr(thd)_4 was confirmed by melting point determination, carbon and hydrogen elemental analysis and proton nuclear magnetic resonance spectrometer (NMR). The MOCVD ZrO_2 film deposition rates were very small (≤ 1 nm/min) for substrate temperatures below 530°C . The film deposition rates were significantly affected by: (1) source temperature, (2) substrate temperature, and (3) total pressure. As-deposited films are carbon free. Furthermore, only the tetragonal ZrO_2 phase was identified in as-deposited films. The tetragonal phase transformed progressively into the monoclinic phase as the films were subjected to high temperature post-deposition annealing. The optical properties of the ZrO_2 thin films as a function of wavelength, in the range of 200 nm to 2000 nm, were also reported. In addition, a simplified theoretical model which considers only a surface reaction was used to analyze the deposition of ZrO_2 film. The deposition rates can be predicted well for various deposition conditions in the hot wall reactor.

The deposition rates of MOCVD $\text{Bi}_4\text{Ti}_3\text{O}_{12}$ were in the range of 3.9–12.5 nm/min. The Bi/Ti ratio was controlled by precursor temperature, carrier gas flow rate, and deposition temperature. As-deposited films were pure $\text{Bi}_4\text{Ti}_3\text{O}_{12}$ phase. The films were specular and showed uniform and fine-grain morphology. Optical constants as a function of wavelength were calculated from the film transmission characteristics in the UV–VIS–NIR region. The 550°C annealed film had a spontaneous polarization of $26.5\ \mu\text{C}/\text{cm}^2$ and a coercive field of $244.3\ \text{kV}/\text{cm}$.

ACKNOWLEDGEMENTS

I wish to express my gratitude to my advisor Dr. S. B. Desu for his professional guidance and support throughout my graduate work. It has been my honor to be a student of such a distinguished scholar with a great wealth of academic knowledge, enthusiasm and ambition.

I thank Dr. C. W. Spencer, Dr. G. Q. Lu , and Dr. W. T. Reynolds, Jr. for agreeing to be on my committee and providing me with valuable advice and good suggestions during this research work.

I am grateful to Dr. C. H. Peng for his kind help in MOCVD, optical measurements, and for many valuable discussions. Special thanks go to: Ching-Yi Tsai for his help in CVD modeling; Justin Gaynor for his help in correcting English errors of the manuscript; Chen-Chung Li for his help in depositing electrodes for electric property measurements; May Nyman for her help in synthesizing precursors; Chien-Chia Chiu for his help in ESCA measurements. I would also like to thank Prof. Z. Chen, Prof. C. Qiu, Dr. I. Yoo, Dr. Chi Kong Kowk, Warren Hendricks, S. W. Park, Dilip Vijay, Ashraf Khan, Jimmy Xing, Claire Chen, Jhing-Fang Chang for many interesting discussion and being good friends.

Many thanks to Frank Cromer and Steve McCartney for their expert help in SEM, ESCA, EDX, STEM. I would also like to acknowledge the secretarial and staff of Materials Science and Engineering Department.

I am extremely indebted to my parents for their constant support. I would also like to thank my husband, Wei Pan, for his love, support, and encouragement.

TABLE OF CONTENT

	PAGE
ABSTRACT	ii
ACKNOWLEDGEMENTS	iv
LIST OF FIGURES	ix
LIST OF TABLES	xi
 CHAPTER 1 INTRODUCTION	 1
1.1 Chemical vapor deposition	1
1.1.1 CVD process	2
1.2 Metalorganic chemical vapor deposition	5
1.2.1 Precursor selection	5
1.3 Ferroelectric bismuth titanate	10
1.4 Ruthenium dioxide	12
1.5 Zirconium dioxide	13
1.6 Objectives	14
1.7 Presentation of results	15
1.8 References	16
 CHAPTER 2 RuO ₂ FILMS BY METALORGANIC CHEMICAL VAPOR DEPOSITION	 21
2.1 Abstract	22
2.2 Introduction	22

2.3	Experimental procedure	24
2.4	Results and discussion	26
2.4.1	Deposition condition and film phase relationship	26
2.4.2	Surface morphology and compositional uniformity of the films	32
2.4.3	Electrical resistivities and reflective spectrum of RuO_2 films	32
2.5	Summary	36
2.6	References	41

CHAPTER 3 METALORGANIC CHEMICAL VAPOR DEPOSITION

	OF ZrO_2 FILMS USING $\text{Zr}(\text{thd})_4$ AS PRECURSORS	43
3.1	Abstract	44
3.2	Introduction	45
3.3	Experimental procedure	46
3.3.1	Synthesis of $\text{Zr}(\text{thd})_4$	46
3.3.2	MOCVD and characterization of ZrO_2 films	48
3.4	Results and discussion	48
3.4.1	$\text{Zr}(\text{thd})_4$ synthesis	48
3.4.2	MOCVD of ZrO_2 films	49
3.4.3	Characterization of ZrO_2 films	53
3.4.4	Kinetic study of hot-wall MOCVD ZrO_2	61
3.5	Summary	68

3.6 References	73
 CHAPTER 4 FERROELECTRIC BISMUTH TITANATE FILMS BY HOT WALL METALORGANIC CHEMICAL VAPOR DEPOSITION	
4.1 Abstract	77
4.2 Introduction	77
4.3 Experimental procedure	79
4.4 Results and discussion	79
4.5 Summary	91
4.6 References	94
 CHAPTER 5 SUMMARY	 96
 VITA	 98

LIST OF FIGURES

- Figure 1.1 Scheme to show the transport and reaction processes underlying CVD.
- Figure 1.2 Schematic drawing of $\text{Bi}_4\text{Ti}_3\text{O}_{12}$ crystal structure.
- Figure 2.1 Schematic diagram of apparatus for MOCVD RuO_2 thin films.
- Figure 2.2 XRD patterns of MOCVD Ru, RuO_2/Ru , and RuO_2 films on SiO_2/Si substrates.
Deposition conditions are:
(a) $T_d=575^\circ\text{C}$, reactant gas(O_2) flow rate=500 sccm, $T_b=170^\circ\text{C}$
(b) $T_d=575^\circ\text{C}$, reactant gas(O_2) flow rate=500 sccm, $T_b=140^\circ\text{C}$
(c) $T_d=550^\circ\text{C}$, reactant gas(O_2) flow rate=1000 sccm, $T_b=140^\circ\text{C}$,
Other MOCVD parameters are: $P_{\text{total}}=5$ torr, carrier gas(N_2)=5 sccm.
- Figure 2.3 XRD patterns of as-deposited films on (a) quartz, (b) SiO_2/Si , (c) Si substrates under the deposition condition: $T_d=550^\circ\text{C}$, reactant gas(O_2) flow rate=1000 sccm, $T_b=145^\circ\text{C}$, $P_{\text{total}}=5$ torr, carrier gas(N_2)=5 sccm.
- Figure 2.4 XRD patterns of as-deposited MOCVD RuO_2 films on (a) SiO_2/Si , (b) Si, (c) quartz substrates. Deposition conditions are the same as in Fig.3, except $T_b=140^\circ\text{C}$.
- Figure 2.5 SEM micrographs of as-deposited MOCVD RuO_2 film on (a) quartz, and (b) Si (c) SiO_2/Si substrates.
- Figure 2.6 Auger depth profile of as-deposited MOCVD RuO_2 film on Si.
- Figure 2.7 Resistivity of MOCVD RuO_2 film on quartz as a function of temperature.
- Figure 2.8 Resistivity of MOCVD RuO_2 film on quartz as a function of annealing temperature.
- Figure 2.9 Specular reflectance spectrum of as-deposited MOCVD RuO_2 film on quartz.
- Figure 3.1 $\text{Zr}(\text{thd})_4$ synthesis apparatus.
- Figure 3.2 Vapor pressure of $\text{Zr}(\text{thd})_4$ as a function of temperature [6].
- Figure 3.3 Deposition rate as functions of substrate and source temperature.
- Figure 3.4 Deposition rate as a function of total pressure.
- Figure 3.5 SEM micrograph of 1000°C annealed ZrO_2 film on Si substrate.

Figure 3.6	ESCA spectra of ZrO_2 film (a) before sputtering, (b) after sputtering.
Figure 3.7	X-ray Diffraction pattern of MOCVD ZrO_2 film.
Figure 3.8	FTIR spectra of MOCVD ZrO_2 film.
Figure 3.9	Specular transmission spectra of the MOCVD ZrO_2 film on fused quartz.
Figure 3.10	Variation of refractive index with wavelength.
Figure 3.11	The measured temperature profiles of the MOCVD reactor.
Figure 3.12(a)	Deposition rates of ZrO_2 film versus deposition temperatures at position 1.
Figure 3.12(b)	Deposition rates of ZrO_2 film versus deposition temperatures at position 2.
Figure 3.12(c)	Deposition rates of ZrO_2 film versus deposition temperatures at position 3.
Figure 3.13(a)	Comparison of the experimental results with the modeling data.
Figure 3.13(b)	Comparison of the experimental results with the modeling data.
Figure 4.1	Schematic diagram of apparatus for MOCVD $\text{Bi}_4\text{Ti}_3\text{O}_{12}$ thin films.
Figure 4.2	Variation of thin film composition with source temperature and carrier gas flow rate.
Figure 4.3	Variation of thin film composition with substrate temperature.
Figure 4.4	SEM micrographs of MOCVD $\text{Bi}_4\text{Ti}_3\text{O}_{12}$ thin film annealed at 550°C : (a) on Si, (b) on Pt/Ti/ SiO_2 /Si, (c) on sapphire substrates
Figure 4.5	X-ray diffraction patterns of the $\text{Bi}_4\text{Ti}_3\text{O}_{12}$ Film at different post-deposition annealing temperature.
Figure 4.6	AES depth profile of 550°C annealed MOCVD $\text{Bi}_4\text{Ti}_3\text{O}_{12}$ film.
Figure 4.7	Typical D-E hysteresis loop of MOCVD $\text{Bi}_4\text{Ti}_3\text{O}_{12}$ film.
Figure 4.8	Optical transmission and reflection spectrum of MOCVD $\text{Bi}_4\text{Ti}_3\text{O}_{12}$ film on sapphire substrate.
Figure 4.9	Variation of refractive index and extinction coefficient of MOCVD $\text{Bi}_4\text{Ti}_3\text{O}_{12}$ film with wavelength.

LIST OF TABLES

Table 1.1	Possible selection of metalorganic precursors and their selected properties for $\text{Bi}_4\text{Ti}_3\text{O}_{12}$ films.
Table 1.2	Possible selection of metalorganic precursors and their selected properties for RuO_2 films.
Table 1.3	Possible selection of metalorganic precursors and their selected properties for ZrO_2 films.
Table 2.1	Typical deposition conditions for MOCVD RuO_2 thin films.
Table 4.1	Typical deposition conditions for MOCVD $\text{Bi}_4\text{Ti}_3\text{O}_{12}$ thin films.

CHAPTER 1 INTRODUCTION

1.1 CHEMICAL VAPOR DEPOSITION

Chemical vapor deposition (CVD) is a process in which a thin solid film is deposited from the gaseous phase by a chemical reaction. Traditional CVD processes are initiated by the input of thermal energy to the substrate and carried out in atmospheric pressures. Alternative methods of energy input include plasma and high frequency radiation, which are known as plasma-enhanced CVD and photo CVD, respectively. CVD can also be categorized according to the pressure at which deposition is carried out. Terms such as reduced pressure CVD, low pressure CVD, and ultrahigh vacuum CVD are used.

Compared to other thin film deposition techniques such as sputtering, pulsed laser ablation, molecular beam epitaxy(MBE), and sol-gel processing, CVD often offers superior deposition rates, step coverage, and composition control. Purity, controllability, and precision have been demonstrated by CVD which are competitive with the MBE technique. More importantly, CVD is capable of producing materials for an entire class of devices which utilize either ultra-thin layers or atomically sharp interfaces. Therefore, it has been considered very promising and has found a variety of applications. The four main areas of

application are microelectronics, optoelectronics, protective and decorative coatings, and optical coatings.

1.1.1 CVD process

A variety of CVD reactors have been designed to meet particular applications. A typical CVD system consists of three basic parts, which serve the following purposes: formation of precursor gases, deposition, and exhaust.

The individual steps in a CVD process can be displayed schematically in Fig 1.1 [1] and summarized as following:

- (1) mass transport of the reactant in the gas flow region from the reactor inlet to the deposition zone;
- (2) gas phase reactions leading to the formation of precursors and byproducts;
- (3) mass transport of precursors to the growth surface;
- (4) adsorption of precursors on the growth surface;
- (5) surface diffusion of precursors to growth sites;
- (6) incorporation of constituents into the growing film;
- (7) desorption of byproducts of the surface reactions; and
- (8) mass transport of byproducts away from the deposition zone towards the reactor exit [1].

The basic physicochemical processes underlying CVD are chemical reactions, nucleation and growth, and transport phenomena.

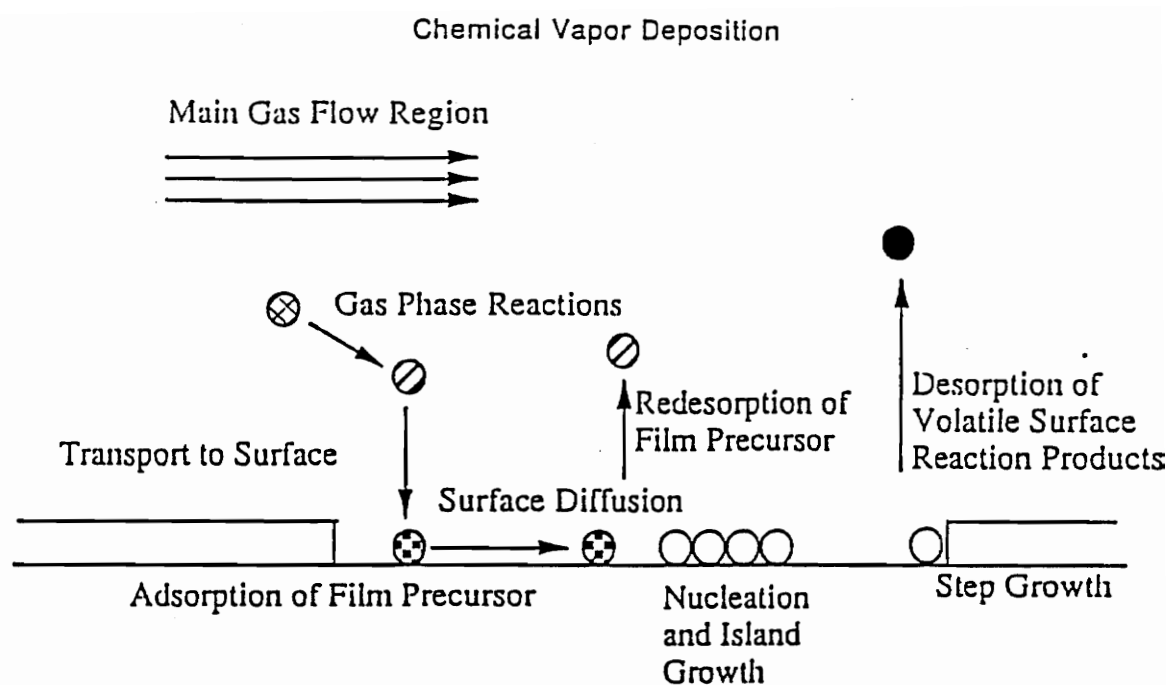


Fig. 1.1 Scheme to show the transport and reaction processes underlying CVD [1].

Chemical reactions involved in CVD processes are very complex and usually include both gas-phase and surface reactions. The various reaction schemes are pyrolysis, reduction, oxidation, and disproportionation of the reactants. The fundamental reaction pathways and kinetics are difficult to investigate, except for only a few well characterized, industrially important systems(e.g. silicon deposition).

The nucleation processes and film growth rates are mainly influenced by the gas-phase composition and substrate temperature. The former influences the film nucleation rate, whereas the latter affects the growth rate. Single-crystal growth is favored by low gas supersaturation and high substrate temperatures, whereas amorphous film formation is promoted at the opposite extremes. Nucleation occurs at many different points on the surface at intermediate temperatures and growth rates. Adsorbed species then diffuse to the islands which grow and coalesce to form a polycrystalline film. The presence of impurities increases the nucleation density and shifts the transition of epitaxy to higher substrate temperatures.

Transport phenomena in a CVD process include fluid flow, heat transfer, and mass transfer. These processes are important because they influence both the access of precursors to the substrate and the gas-phase reactions taking place before deposition, which, in turn, affects film thickness and composition uniformity. The complex reactor geometries, inlet nozzles, and exhaust manifolds lead to a wide variety of flow structures. Nevertheless basic insights can be gained through flow visualizations and computer simulations on appropriately chosen model systems.

1.2 METALORGANIC CHEMICAL VAPOR DEPOSITION

For many years precursors for materials deposited by CVD have been restricted to widely available simple inorganic compounds. However, there has been an increasing demand for more sophisticated deposits, especially of optoelectronic and microelectronic materials, and the need for better control of deposition rates, uniformity, layer properties and quality. In recent years, metalorganic precursors where the metal has been made volatile by bonding it to organic ligands have been extensively investigated. Chemical vapor deposition using metalorganic precursors is called metalorganic chemical vapor deposition (MOCVD).

1.2.1 Precursor selection

The selection of precursors is a crucial step in a MOCVD process for successful deposition of a complex metal oxide thin film. An ideal precursor for MOCVD should have the following properties:

- (1) high vapor pressure at moderately low temperature;
- (2) low decomposition temperature;
- (3) no contamination from the organic constituents of the precursors;
- (4) stability under ambient conditions; and
- (5) non-toxic.

Three classes of metalorganic compounds which have been commonly used as precursors to deposit metal oxide films are metal alkyls ($M^{n+}R_n$), metal alkoxides $[M^{n+}(OR)_n]$, and metal β -diketonates $[M^{n+}(O_2C_3HR_2)_n]$. Most of these

metalorganic precursors have acceptable vapor pressures at moderately low temperatures. Metal alkoxides and metal β -diketonates are easier to handle and much less toxic than their alkyl equivalents, while metal alkyls tend to be more volatile. The physical and chemical properties of the metalorganic precursors can be tailored by changing their chemical structure. In other words, the nature, bulkiness, branching, or fluorine substitution of the organic R-group can significantly affect properties such as volatility and stability.

A selection of metalorganic precursors which have appeared in the literature for the deposition of $\text{Bi}_4\text{Ti}_3\text{O}_{12}$ are listed in Table 1.1 [2–14]. Titanium alkoxides have been used as precursors for TiO_2 thin film deposition without significant disadvantages. They are reasonably stable under ambient conditions, and do not present any extreme health hazards. $\text{Ti}(\text{OEt})_4$ is chosen in the deposition of $\text{Bi}_4\text{Ti}_3\text{O}_{12}$ in this study.

The precursors studied for the deposition of RuO_2 films are listed in Table 1.2. Films deposited from $\text{Ru}_3(\text{CO})_{12}$ consisted entirely of Ru, regardless of the O_2 , ambient gas composition in the reactor. Inferior quality RuO_2 films obtained from $\text{Ru}(\text{C}_5\text{H}_7\text{O}_2)_3$ consisted of large columnar grains which resulted in a very high electrical resistivity of $643\ \mu\Omega\text{--cm}$. Only $\text{Ru}(\text{C}_5\text{H}_5)_2$ was found to be promising [15].

The possible selection of metalorganic precursors for ZrO_2 film deposition are listed in Table 1.3 [4–10,16]. The alkoxides $\text{Zr}(\text{OPr}^i)_4$, and $\text{Zr}(\text{OBut})_4$ are not suitable as precursors due to their instabilities [16]. Although good quality ZrO_2 films were obtained using $\text{Zr}(\text{tfa})_4$, the process parameter space is limited because of

Table 1.1 Possible selection of metalorganic precursors and their selected properties for $\text{Bi}_4\text{Ti}_3\text{O}_{12}$ films.

Name	Formula	Abbreviation				
Triphenylbismuth	$\text{Bi}(\text{C}_6\text{H}_5)_3$					
Titanium ethoxide	$\text{Ti}(\text{OC}_2\text{H}_5)_4$	$\text{Ti}(\text{OEt})_4$				
Titanium isopropoxide	$\text{Ti}(\text{O}^i\text{C}_3\text{H}_7)_4$	$\text{Ti}(\text{OPr}^i)_4$ or TIP				
Titanium (di-isopropoxide)-bis(acetylacetonate)	$\text{Ti}(\text{C}_5\text{H}_7\text{O}_2)_2(\text{O}^i\text{C}_3\text{H}_7)_2$	$\text{Ti}(\text{acac})_2(\text{OPr}^i)_2$				
Selected Properties						
Precursor	Appearance at RT	Air Stability	Melting Point	Boiling Point	Vaporization Temperature	Decomposition Temperature
	White crystal		77–78°C	310°C		
$\text{Ti}(\text{OEt})_4$	Colorless Lq	Stable	—	122°C	110°C	300°C
TIP	Colorless Lq		20°C	58°C	25°C – 106°C	—
$\text{Ti}(\text{acac})_2$						
$(\text{OPr}^i)_2$	Orange Lq.		—	—	87°C	—

Table 1.2 Possible selection of metalorganic precursors and their selected properties for
RuO₂ films

Name	Formula	Appearance at RT	Melting Point
Bis(cyclopentadienyl)- ruthenium (Ruthenocene)	$\text{Ru}(\text{C}_5\text{H}_5)_2$	Light yellow crystal	194–198°C
Ruthenium (III) acetylacetonate	$\text{Ru}(\text{C}_5\text{H}_7\text{O}_2)_3$	Red–brown crystal	230–235°C
Ruthenium carbonyl	$\text{Ru}_3(\text{CO})_{12}$	Orange crystal	150°C

Table 1.3 Possible selection of metalorganic precursors and their selected properties for ZrO_2 films.

Name	Formula	Abbreviation
Zirconium isopropoxide	$\text{Zr}(\text{O}^i\text{C}_3\text{H}_7)_4$	$\text{Zr}(\text{OPr}^i)_4$ or ZIP
Zirconium t-butoxide	$\text{Zr}(\text{O}^t\text{C}_4\text{H}_9)_4$	$\text{Zr}(\text{OBu}^t)_4$ or ZTB
Zirconium acetylacetonate	$\text{Zr}(\text{C}_5\text{H}_7\text{O}_2)_4$	$\text{Zr}(\text{acac})_4$
Zirconium trifluoroacetylacetonate	$\text{Zr}(\text{C}_5\text{H}_4\text{F}_3\text{O}_2)_4$	$\text{Zr}(\text{tfa})_4$
Zirconium tetramethylheptadione	$\text{Zr}(\text{C}_{11}\text{H}_{19}\text{O}_2)_4$	$\text{Zr}(\text{dpm})_4$ or $\text{Zr}(\text{thd})_4$

Selected properties						
Precursor	Appearance at RT	Air Stability	Melting Point	Boiling Point	Vaporization Temperature	Decomposition Temperature
ZIP	Lq.	Sensitive	—	—	175°C	—
ZTB	Yellow Lq.	Sensitive	—	95°C	25°C – 50°C	—
$\text{Zr}(\text{acac})_4$	White Powder	Sensitive	173°C	—	160°C	300°C
$\text{Zr}(\text{tfa})_4$	White Powder	Sensitive	128°C	235°C	160°C	300°C
$\text{Zr}(\text{thd})_4$	White Powder	Stable	345°C	—	180°C – 230°C	500 – 550°C

possible fluorine contamination. ZrO_2 films have a high carbon contamination of 15 atom% when $\text{Zr}(\text{acac})_4$ is used [16]. On the other hand, $\text{Zr}(\text{thd})_4$ is thermally stable over its vaporization temperature range and is very easy to handle under ambient conditions [10].

1.3 FERROELECTRIC BISMUTH TITANATE

Ferroelectric materials exhibit a characteristic temperature, the Curie temperature, at which the materials make a structural phase change from a polar phase (ferroelectric phase) to a non-polar phase (paraelectric phase). One of the well-known features of ferroelectric materials is the response of the polarization to the external electric field, which is often referred to as the hysteresis loop or hysteresis curve.

$\text{Bi}_4\text{Ti}_3\text{O}_{12}$ is a typical ferroelectric material and has a polar orthorhombic structure with B2cb, $a = 5.448$, $b = 5.411$, $c = 32.83$ and $Z = 4$. A schematic drawing of the $\text{Bi}_4\text{Ti}_3\text{O}_{12}$ crystal structure is shown in Fig. 1.2, where A is the perovskite layer, B is a unit cell of hypothetical perovskite structure, and C is $(\text{Bi}_2\text{O}_2)^{2+}$ layers [17]. The polarization vector in $\text{Bi}_4\text{Ti}_3\text{O}_{12}$ is inclined at a small angle ($\sim 4.5^\circ$) to the a - b plane which leads to two polarization moments: one along the a axis, $P_s = 50 \mu\text{C}/\text{cm}^2$, and the other along the c axis, $P_s = 4 \mu\text{C}/\text{cm}^2$, with coercive fields of 50 and 3–5 kV/cm, respectively [17].

$\text{Bi}_4\text{Ti}_3\text{O}_{12}$ exhibits useful properties for nonvolatile memory, piezoelectric, and electro-optic devices [18] because of its relatively high dielectric constant, high

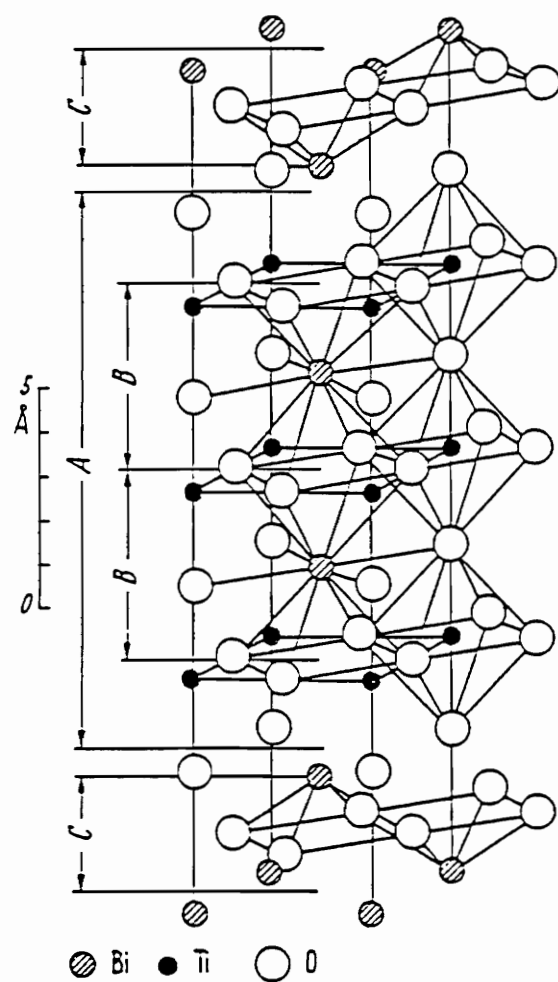


Figure 1.2 Schematic drawing of $\text{Bi}_4\text{Ti}_3\text{O}_{12}$ crystal structure.

Curie temperature (675°C), and high breakdown strength. The low coercive field along the c axis makes $\text{Bi}_4\text{Ti}_3\text{O}_{12}$ even more attractive. Recently, epitaxial $\text{Bi}_4\text{Ti}_3\text{O}_{12}$ thin films have been successfully grown by pulsed excimer laser deposition on $\text{SrTiO}_3(100)$ [19], $\text{MgO}(110)$ [20], and $\text{YBa}_2\text{Cu}_3\text{O}_7(001)$ [21].

1.4 RUTHENIUM DIOXIDE

Recent advances in ferroelectric thin film materials and devices have brought the realization of nonvolatile, high packing density, radiation hard, high speed, random access computer memories close to commercial reality [22]. However, present techniques still require that technical obstacles be overcome if ferroelectric memory devices are to gain widespread acceptance. The major problems that plague ferroelectric memories, based most commonly on lead zirconate titanate materials, are degradation properties such as fatigue, aging, and electrical degradation, including low voltage breakdown. It is believed that oxygen is a common source of fatigue, aging, and electrical degradation [23,24]. Therefore, the quality of the interface between the electrode and ferroelectric layer has a significant impact on the device degradation characteristics. Thus, the criteria for electrode material selection should be chemical inertness, electrical conductivity, and most important of all, structurally matching to the ferroelectric material in order to minimize interfacial defect formation. In addition, the electrode material should be able to be integrated into the existing silicon VLSI technology.

The metallic oxides of transition metals such as ruthenium, rhodium, iridium, and osmium are promising candidates for various VLSI metallization

schemes primarily because of their low resistivity and high thermal stability [25]. Dioxides of these materials have bulk resistivities in the range of 30 – 100 $\mu\Omega$ –cm. They crystallize in the tetragonal rutile structure and some of these oxides such as RuO_2 exhibit excellent diffusion barrier properties. The improvement in ferroelectric properties of the ferroelectric capacitor using RuO_2 as an electrode has been reported by several authors [26,27]. It was found that the use of RuO_2 as electrodes for ferroelectric capacitors reduced the lattice mismatch and work function difference at the interface, thereby reducing the defect entrapment and subsequent loss of polarization in the ferroelectric material [26]. In addition, success in removing RuO_2 electrode was reported by using reactive ion etching [28].

1.5 ZIRCONIUM DIOXIDE

Zirconium dioxide (Zirconia) has three polymorphic phases: monoclinic at room temperature, tetragonal at 1100 °C, and cubic at 2285 °C [29]. Normally, the high temperature forms can not be quenched, yet, surprisingly, they were found to exist at room temperature [30]. Garvie advanced the hypothesis that the occurrence of the metastable high temperature phases could be accounted for as a crystalline size effect [30]. Stabilization of the high temperature phases can be achieved by additions of oxides such as Y_2O_3 , MgO , and CeO [29]. The wide variety of applications of zirconia stems from its basic property of polymorphism.

Thin films of zirconia find applications in many fields of interest such as thermal barrier coatings, laser coatings, multilayer optical coatings, etc. More recently, its use as a buffer layer for superconducting coatings has been established

[31,32].

ZrO₂ films used as thermal barrier coatings are fabricated by the plasma spray process. The ZrO₂ barrier coatings possess desirable properties such as high thermal expansion coefficient, low thermal conductivity, chemical stability in the turbine environment and thermal shock resistance [29].

ZrO₂ films have been employed as substrates for various thin film deposition and patterning schemes requiring laser interaction because of their resistance to laser damage [33]. This utility of ZrO₂ derives from its high transmittance, high melting point, large optical bandgap (5 eV), high index of refraction (≈ 2), strong Zr–O bonding, and chemical inertness.

Zirconia film is of interest as a high refractive index material in multilayer optical coatings because of its low absorption in a broad spectral region from the near–UV to the mid–IR [34]. In addition to having a large optical band gap and a high laser damage threshold, it is hard, durable, and easily available. Therefore, it is suitable for making high reflecting mirrors, laser gyros, and broadband interference filters [33].

1.6 OBJECTIVES

The principal objectives of this study were to:

- (1) study the MOCVD processes of various simple oxide thin films, namely ZrO₂ and RuO₂.

- (2) study the MOCVD processes of complex oxide thin films, namely $\text{Bi}_4/\text{Ti}_3\text{O}_{12}$.
- (3) investigate the structure, composition, optical properties and electrical properties of MOCVD ZrO_2 , RuO_2 , and $\text{Bi}_4\text{Ti}_3\text{O}_{12}$ thin films.

1.7 PRESENTATION OF RESULTS

The results of this study are presented in the form of journal publications, which appear as separate chapters (chapter 2 to 4) following the introduction. It should be noted that each chapter is complete within itself, i.e. it has its own introduction, theory, results, discussions, summaries and references. The overall summary of the entire study is given in chapter 5.

1.8 REFERENCES

1. Michael L. Hitchman, and Klavs F. Jensen, "Chemical Vapor Deposition, principles and applications", (Academic press, New York, 1993).
2. S. Yuhya, K. Kikuchi, M. Yoshida, K. Sugawara, and Y. Shiohara, "Volatilities of Precursors for Chemical Vapor Deposition of Superconducting Thin Films," Mol. Cryst. Liq. Cryst., 184, 231 (1990).
3. T. Hashimoto, T. Kosaka, Y. Yoshida, and H. Koinuma, "Microwave Plasma CVD of Oxide Films Relating to High-T_c Bi-Sr-Ca-Cu-O Superconductor," Mol. Cryst. Liq. Cryst., 184, 207 (1990).
4. M. Okada, K. Tominaga, T. Araki, S. Katayama, and Y. Sakashita, "Metalorganic Chemical Vapor Deposition of c-axis Oriented PZT Thin Films," Jpn. J. Appl. Phys., 29(4), 718 (1990).
5. Y. Sakashita, T. Ono, H. Segawa, K. Tominaga, and M. Okada, "Preparation and Electrical Properties of MOCVD-Deposited PZT Thin Films," J. Appl. Phys., 69(12), 8352 (1991).
6. H. Funakubo, K. Imashita, N. Kieda, and N. Mizutani, "Formation of Epitaxial Pb(Zr,Ti)O₃ Film by CVD," J. Ceram. Soc. Jpn., 99, 241 (1991).
7. K. Kashiwara, H. Itoh, K. Tsukamoto, and Y. Akasaka, "Formation of PZT

Films by MOCVD," Extended Abstracts of the 1991 International Conference on Solid State Devices and Materials(Yokohama, Japan), 192 (1991).

8. G. J. M. Dormans, M. de Keijser, and P. J. van Veldhoven, "Ferroelectric $\text{PbZr}_x\text{Ti}_{1-x}\text{O}_3$ Thin Films Grown by Organometallic Chemical Vapor Deposition," Mat. Res. Soc. Symp. Proc., 243, 203 (1992).

9. C. H. Peng and S. B. Desu, "Low-Temperature Metalorganic Chemical Vapor Deposition of Perovskite $\text{Pb}(\text{Zr}_x\text{Ti}_{1-x})\text{O}_3$ Thin Films," Appl. Phys. Lett., 61(1), 16 (1992).

10. M. Nyman, "Synthesis and Characterization of Precursors for Chemical Vapor Deposition of Metal Oxide Thin Films," M.S. Thesis, Virginia polytechnic institute and state university, July 1992.

11. F. W. Ainger, C. J. Brierley, M. D. Hudson, C. Trundle, and R. W. Whatmore, "Ferroelectric Thin Films by Metalorganic Chemical Vapor Deposition," Mat. Res. Soc. Symp. Proc., 200, 37 (1991).

12. C. J. Brierley, C. Trundle, L. Considine, R. W. Whatmore, and F. W. Ainger, "The Growth of Ferroelectric Oxides by MOCVD," Ferroelectrics, 91,181 (1989).

13. B. S. Kwak, E. P. Boyd, and A. Erbil, "Metalorganic Chemical Vapor Deposition of PbTiO_3 Thin Films," Appl. Phys. Lett., 53(18), 1702 (1989).

14. S. L. Swartz, D. A. Seifert, G. T. Noel, and T. R. Shrout, " Characterization of MOCVD PbTiO_3 Thin Films," *Ferroelectrics*, 93, 37 (1989).
15. M. L. Green, M. E. Gross, L. E. Papa, K. J. Schnoes, and D. Brasen, "Chemical Vapor Deposition of Ruthenium and Ruthenium Dioxide Films," *J. Electrochem. Soc.*, 132(11), 2677 (1985).
16. S. B. Desu, S. Tian, and C. K. Kwok, "Structure, Composition, and Properties of MOCVD ZrO_2 Thin Films," *Mat. Res. Soc. Symp. Proc.*, 168, 349 (1990).
17. T. Mitsui and E. Nakamura (Editors), *Landolt–Bornstein Series, Vol. 28 Ferroelectrics and Related Substance*, (Springer–Verlag, Berlin, 1990).
18. S. Y. Wu, W. J. Takei, and M. H. Francombe, "Optical Switching Characteristics of Epitaxial Bismuth Titanate Films for Matrix–Addressed Displays," *Ferroelectrics*, 10, 209 (1976).
19. R. Ramesh, K. Luther, B. Wiken, D. L. Hart, E. Wang, J. M. Tarascon, A. Inam, X. D. Wu, and T. Venkatesan, "Epitaxial Growth of Ferroelectric Bismuth Titanate Thin Films by Pulsed Laser Deposition," *Appl. Phys. Lett.*, 57, 1505 (1990).
20. H. Buhay, S. Sinharoy, W. H. Kasner, M. H. Farancombe, D. R. Lampe, and E. Stepke, "Pulsed Laser Deposition and Ferroelectric Characterization of Bismuth Titanate Films," *Appl. Phys. Lett.*, 58, 1470 (1991).

21. R. Ramesh, A. Inam, B. Wilkens, W. K. Chan, T. Sands, D. K. Fork, T. H. Geballe, J. Evans, and J. Bullingyon, "Ferroelectric Bismuth Titanat/Superconductor (Y–Ba–Cu–O) Thin Film Heterostructures on Silicon," *Appl. Phys. Lett.*, 59, 1782 (1991).
22. 5th International Symposium on Integrated Ferroelectrics held on April 19 – 21, 1993 in Colorado Springs, Colorado.
23. I. K. Yoo and S. B. Desu, "Mechanism of Fatigue in Ferroelectric Thin Films," *Phys. Stat. Sol. (a)*, 133, 565 (1992).
24. I. K. Yoo and S. B. Desu, "Fatigue Modeling of Lead Zirconate Titanate Thin Films," *Mater. Sci. Eng.*, B13, 319 (1992).
25. L. Krusin–Elbaum and M. Wittmer, "Conducting Transition Metal Oxides: Possibilities for RuO₂ in VLSI Metallization," *J. Electrochem. Soc.: Solid State Science and Technology*, 135, 2610 (1988).
26. C. K. Kwok, D. P. Vijay, S. B. Desu, N. R. Parikh, and E. A. Hill, "Conducting Oxide Electrodes for Ferroelectric Films," *Proceedings of ISIF '92*, 412 (1992).
27. S. D. Bernstein, T. Y. Wong, Y. Kisler, and R. W. Tustison, "Fatigue of Ferroelectric PbZr_xTi_yO₃ Capacitors with Ru and RuO_x Electrodes," *J. Mater. Res.*, 8, 12 (1993).

28. S. B. Desu and W. Pan, "Reactive Ion Etching of $\text{PbZr}_{1-x}\text{Ti}_x\text{O}_3$ and RuO_2 Films by Environmentally Safe Gases," submitted to Science.
29. R. Stevens, Zirconia and zirconia ceramics, (Magnesium Elektron Ltd., 1986).
30. R. C. Garvie, "Stabilization of the Tetragonal Structure in Zirconia Microcrystals," J. Phys. Chem., 82(2), 218 (1978).
31. T. Venkatesan, D. W. Chase, X. D. Wu, A. Inam, C. Change, and F. Shokoohi, "Superconducting $\text{Y}_1\text{Ba}_2\text{Cu}_3\text{O}_{7-x}$ Films on Si," Appl. Phys. Lett., 53, 243 (1988).
32. I. El Shanshoury, V. Rudenko, and I. Ibrahim, "Polymorphic Behavior of Thin Evaporated Films of Zirconium and Hafnium Oxides," J. Am. Ceram. Soc., 53, 264 (1970).
33. W. H. Llowdermilk, D. Milam, and F. Rainer, "Optical Coatings for Laser Fusion Applications," Thin Solid Films, 73, 155 (1980).
34. A. Duparre, E. Welsch, H. —G. Walther, N. Kaiser, H. Muller, E. Hacker, H. Lauth, J. Meyer, and P. Weissbrodt, "Structure—Related Bulk Losses in ZrO_2 Optical Thin Films," Thin Solid Films, 187, 275 (1990).

This paper entitled

**RuO₂ FILMS BY METALORGANIC CHEMICAL VAPOR
DEPOSITION**

has been accepted for publication in

JOURNAL OF MATERIALS RESEARCH

CHAPTER 2 RuO₂ FILMS BY METALORGANIC CHEMICAL VAPOR DEPOSITION

2.1 ABSTRACT

Pure and conducting RuO₂ thin films were successfully deposited on Si, SiO₂/Si and quartz substrates at temperatures as low as 550°C by a hot wall metalorganic chemical vapor deposition (MOCVD). Bis(cyclopentadienyl)ruthenium, Ru(C₅H₅)₂, was used as the precursor. An optimized MOCVD process for conducting RuO₂ thin films was established. Film structure was dependent on MOCVD process parameters such as bubbler temperature, dilute gas flow rates, deposition temperature, and total pressure. Either pure RuO₂, pure Ru, or a RuO₂ + Ru mixture was obtained under different deposition conditions. As-deposited pure RuO₂ films were specular, crack-free, and well adhered on the substrates. The Auger electron spectroscopy depth profile showed good composition uniformity across the bulk of the films. The MOCVD RuO₂ thin films exhibited a resistivity as low as 60 μΩ-cm. In addition, the reflectance of RuO₂ in the NIR region had a metallic character.

2.2 INTRODUCTION

Ruthenium dioxide (RuO_2), a transition metal dioxide with rutile structure, has very interesting properties such as low resistivity ($\rho = 46 \mu\Omega\text{-cm}$) and high thermodynamic stability which are the basis for a variety of applications. RuO_2 has been well known as a corrosion-resistant electrode for chlorine or oxygen evolution [1]. In a recent research, RuO_2 thin films have shown great promise in several different VLSI metallization schemes [2,3]. In addition, we have recently shown that RuO_2 is a very good metallization contact for ferroelectric lead titanate zirconate (PZT) films [4]. The use of RuO_2 reduced the lattice mismatch and work function difference at the interface, and consequently reduced the defect entrapment, loss of polarization, and improved fatigue lifetime [4]. Furthermore, RuO_2 exhibits excellent diffusion barrier properties. Green, et al. demonstrated that RuO_2 is an effective diffusion barrier against interdiffusion of Al and Si to annealing temperatures as high as 600°C [5]. RuO_2 was also suggested as a buffer layer for YBCO superconducting thin film for reducing interdiffusion and improving nucleation of the proper phase [6]. RuO_2 thin films for resistor applications have been well documented [7].

RuO_2 thin films have been prepared to date mainly by using RF-reactive sputtering [2,3,6,7], although one paper on the MOCVD of RuO_2 film was reported [5]. A problem associated with the sputtered films is high film stress. It was found that the intrinsic stress of each of the sputtered films was compressive on the order of GPa [2,8]. On the other hand, MOCVD is a valuable alternative method since it offers low cost, easy composition control, high deposition rate, excellent step coverage, and compatibility to large scale processing. However, information on MOCVD of RuO_2 is very scarce. Only Green, et al. have reported the preparation

of MOCVD RuO_2 and Ru thin films [5]. In their study, efforts had been made to select suitable precursors for MOCVD RuO_2 thin films. For example, $\text{Ru}(\text{C}_5\text{H}_5)_2$, $\text{Ru}_3(\text{CO})_{12}$, $\text{Ru}(\text{C}_5\text{H}_7\text{O}_2)_3$, were used for RuO_2 deposition. Films deposited from $\text{Ru}_3(\text{CO})_{12}$ consisted entirely of Ru, regardless of the O_2 , N_2 , or vacuum ambient. Inferior quality RuO_2 films obtained from $\text{Ru}(\text{C}_5\text{H}_7\text{O}_2)_3$ consisted of large columnar grains which resulted in a very high electrical resistivity of $643 \mu\Omega\text{-cm}$. Only $\text{Ru}(\text{C}_5\text{H}_5)_2$ was found to be promising. The film deposited at 575°C on SiO_2 substrate was pure phase RuO_2 and had a relatively high electrical resistivity of $89.9 \mu\Omega\text{-cm}$. However, either Ru or $\text{RuO}_2 + \text{Ru}$ mixture was obtained on Si substrates [5].

The present paper reports on the structure, electrical, and optical properties of hot-wall MOCVD RuO_2 thin films, using $\text{Ru}(\text{C}_5\text{H}_5)_2$ as precursors. The emphasis was placed on the correlation of process parameters and the resulting film structure. We were able to deposit pure phase RuO_2 films with low electrical resistivity ($60 \mu\Omega\text{-cm}$) at 550°C on quartz, SiO_2/Si , and Si substrates.

2.3 EXPERIMENTAL PROCEDURE

RuO_2 thin films were deposited in a MOCVD apparatus which is shown schematically in Fig. 2.1. The precursor, $\text{Ru}(\text{C}_5\text{H}_5)_2$, was kept at the desired temperature within 1°C accuracy. The precursor vapors were delivered into the reactor during deposition using a vacuum pump and 5 sccm of nitrogen carrier gas. Precursor source temperatures in the range of 140 to 170°C were employed to obtain desirable vapor pressures. Pure oxygen was used as the reactant gas with the flow

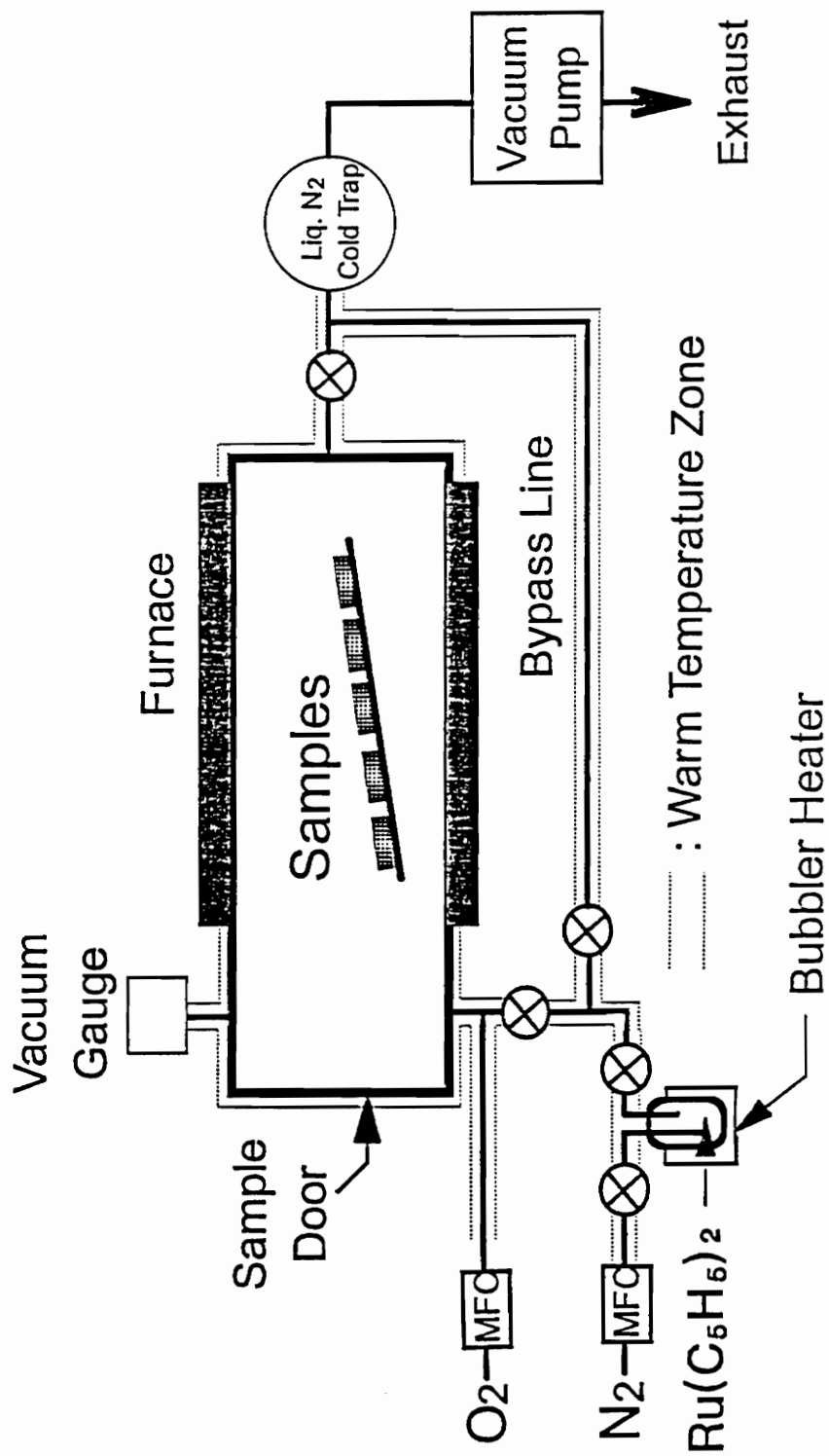


Figure 2.1 Schematic diagram of apparatus for MOCVD RuO_2 thin films.

rates varying from 500 to 1000 sccm. The total pressure varied from 2.5 to 10 torr. The substrates used were SiO₂/Si, quartz, and Si. The deposition temperatures were in the range of 550 to 575°C. The typical deposition conditions are listed in Table 2.1. For the deposition conditions described in Table 2.1, film growth rates were typically around 10 nm/min.

The identification of RuO₂ phases was carried out using an x-ray diffractometer with CuK α radiation. Scanning electron microscopy (SEM) was used to study the surface morphology of the films. The resistivities of the films were determined using a four-point probe method. The reflectance spectra of the film in the UV-VIS-NIR region were obtained from a UV-VIS-NIR scanning spectrophotometer.

2.4 RESULTS AND DISCUSSION

2.4.1 Deposition condition and film phase relationship

In the range of experimental parameters investigated, source temperature, substrate temperature, and reactant gas flow rate were found to affect significantly the crystal structure and composition of the films. Fig. 2.2 shows the XRD patterns of the films deposited on SiO₂/Si under different deposition conditions. As can be seen in Fig. 2.2, pure RuO₂, RuO₂ + Ru mixture, and pure Ru thin films were obtained. For example, under deposition condition (a), i.e. deposition temperature (T_d) = 575°C, dilute gas flow rate = 500 sccm, and bubbler temperature (T_b) = 170°C, the resulting film consisted of pure Ru phase [Fig. 2.2(a)], while under

Table 2.1. Typical deposition conditions for MOCVD RuO₂ thin films

Precursors	Ru(C ₅ H ₅) ₂
Precursors Temp.(°C)	140–170
Carrier Gas(sccm,N ₂)	5
Substrate	Si, SiO ₂ , Quartz
Substrate Temp.(°C)	550–575
Reactant Gas (sccm,O ₂)	500–1000
Total Pressure(torr)	2.5–10

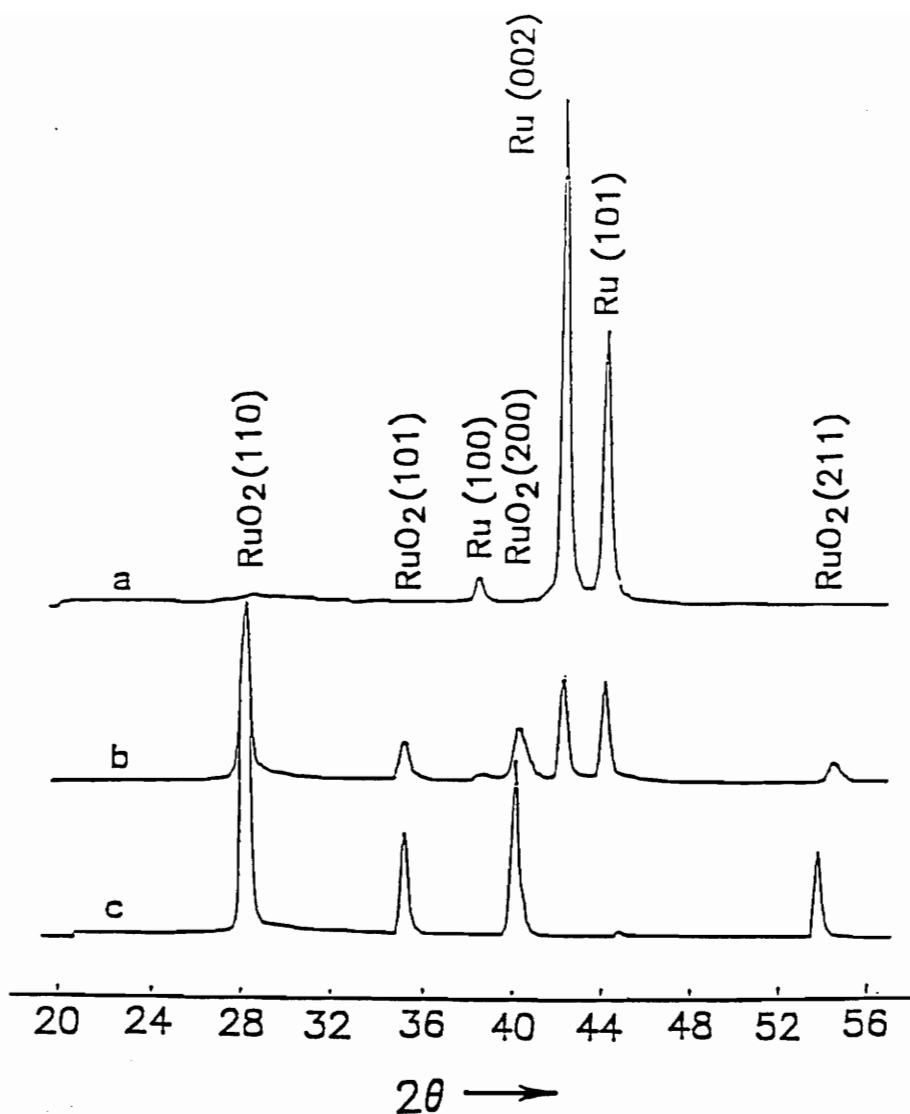


Figure 2.2 XRD patterns of MOCVD Ru, RuO₂/Ru, and RuO₂ films on SiO₂/Si substrates.

Deposition conditions are:

(a) $T_d=575^\circ\text{C}$, reactant gas(O_2) flow rate=500 sccm, $T_b=170^\circ\text{C}$

(b) $T_d=575^\circ\text{C}$, reactant gas(O_2) flow rate=500 sccm, $T_b=140^\circ\text{C}$

(c) $T_d=550^\circ\text{C}$, reactant gas(O_2) flow rate=1000 sccm, $T_b=140^\circ\text{C}$,

Other MOCVD parameters are: $P_{\text{total}}=5$ torr, carrier gas(N_2)=5 sccm.

deposition condition (c), i.e. $T_d = 550^\circ\text{C}$, dilute gas flow rate = 1000 sccm, and $T_b = 140^\circ\text{C}$, pure RuO_2 film was obtained [Fig. 2.2(c)]. The total pressure and the precursor carrier gas flow rate for these three depositions were kept constant at 5 torr and 5 sccm, respectively. The result indicates that RuO_2 phase was formed when the lower deposition temperature, the lower bubbler temperature, and the higher dilute gas flow rate were used. In other words, low deposition rate and excess oxygen favored RuO_2 formation, while high deposition rate favored Ru phase. This may imply that the decomposition rate of the precursor is rapid, while the oxidation rate of the decomposed products is slow. To fully understand the deposition process, a detailed study of the decomposition process of the precursor, i.e. $\text{Ru}(\text{C}_5\text{H}_5)_2$, is needed.

The substrates were also found to have a significant effect on the phase of the films. Fig. 2.3 shows the XRD patterns of the films deposited on three different substrates under the same deposition condition. The deposition condition was $T_d = 550^\circ\text{C}$, $T_b = 145^\circ\text{C}$, total pressure = 5 torr, reactant gas flow rate = 1000 sccm, and carrier gas flow rate = 5 sccm. As can be seen in Fig. 2.3, pure phase RuO_2 was obtained on quartz substrate, RuO_2 with a trace of Ru was obtained on SiO_2/Si substrate, while $\text{RuO}_2 + \text{Ru}$ mixture was obtained on Si substrate. It seemed that the SiO_2 surface (either quartz substrate or SiO_2 coated Si wafer) could promote the formation of the RuO_2 phase. By lowering the film growth rate, i.e. using lower bubbler temperature (140°C), pure phase RuO_2 was obtained on all three substrates, as shown in Fig. 2.4. In addition, no preferred orientation was found for all samples in this study.

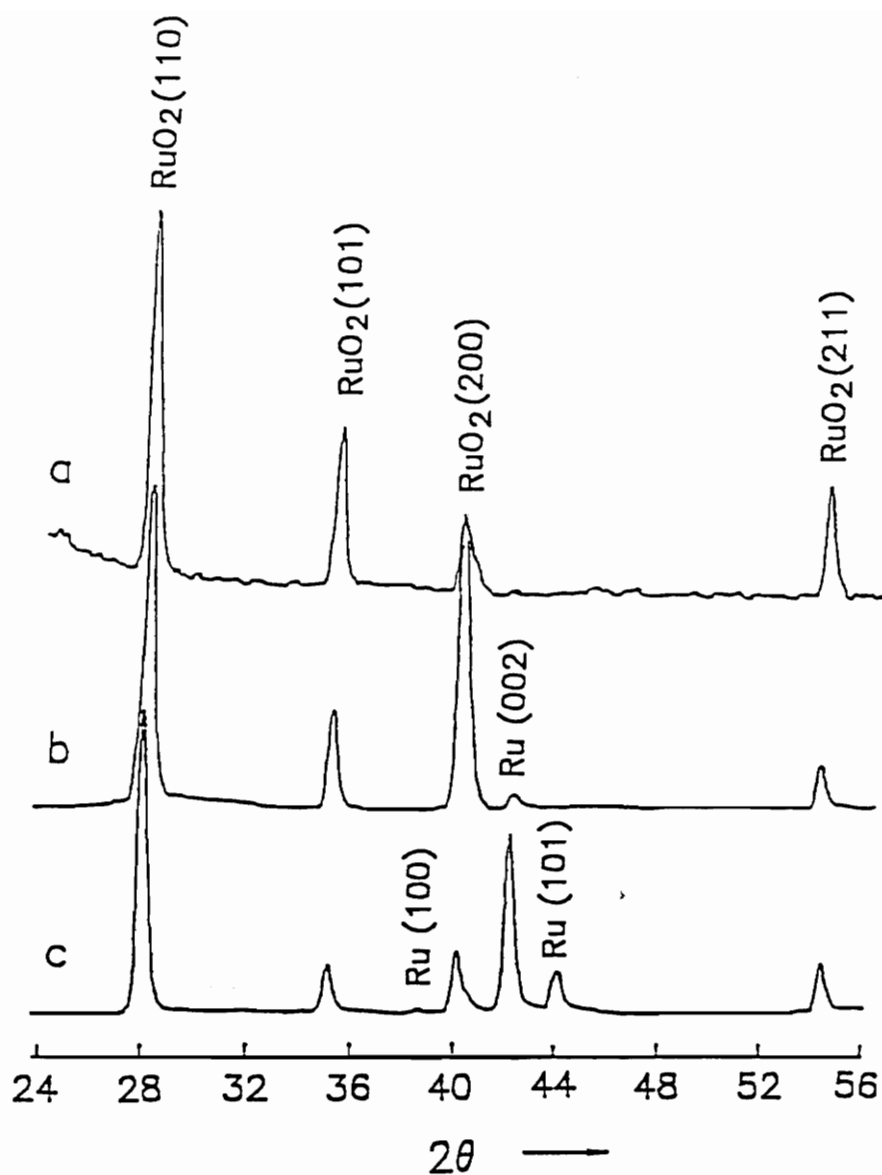


Figure 2.3 XRD patterns of as-deposited films on (a) quartz, (b) SiO_2/Si , (c) Si substrates under the deposition condition: $T_d=550^\circ\text{C}$, reactant gas(O_2) flow rate=1000 sccm, $T_b=145^\circ\text{C}$, $P_{\text{total}}=5$ torr, carrier gas(N_2)=5 sccm.

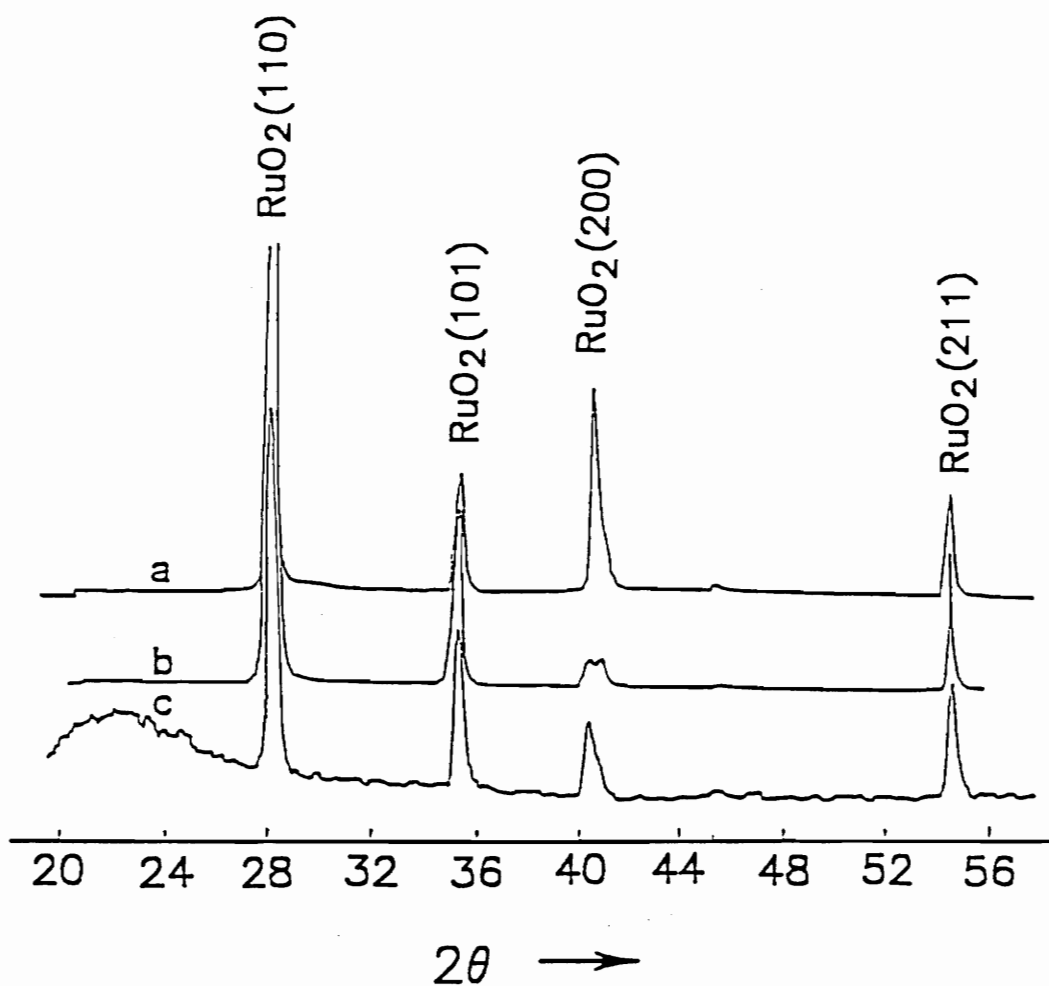


Figure 2.4 XRD patterns of as-deposited MOCVD RuO₂ films on (a) SiO₂/Si, (b) Si, (c) quartz substrates. Deposition conditions are the same as in Fig. 2.3, except $T_b=140^\circ\text{C}$.

The effect of annealing on as-deposited RuO_2 , Ru, and $\text{RuO}_2 + \text{Ru}$ mixture films was also studied. The annealing process was performed in air for 30 min. The phase of these films did not change for annealing temperatures up to 700°C . In other words, Ru did not oxidize under these annealing conditions.

2.4.2 Surface morphology and compositional uniformity of the films

The as-deposited MOCVD RuO_2 films were specular and dark blue in color, crack-free, and were adhered very well on all three substrates used. The surface morphology of the as-deposited MOCVD RuO_2 films on quartz and Si substrates were investigated by SEM and is shown in Fig. 2.5. The average grain size was estimated to be less than $0.3\ \mu\text{m}$.

Auger electron spectroscopy (AES) was used to examine the composition uniformity across the thickness of the film. The AES depth profile of the as-deposited RuO_2 on Si is given in Fig. 2.6. Both oxygen and ruthenium are evenly distributed in the film, suggesting that the composition through the bulk of the film is uniform.

2.4.3 Electrical resistivities and reflective spectrum of RuO_2 films

The room temperature resistivity of the as-deposited MOCVD RuO_2 is about $60\ \mu\Omega\text{-cm}$. It was measured using the four-probe method. The resistivity of the MOCVD RuO_2 film on quartz as a function of temperature is shown in Fig. 2.7. The resistivity of the film increased with the increasing temperature. The

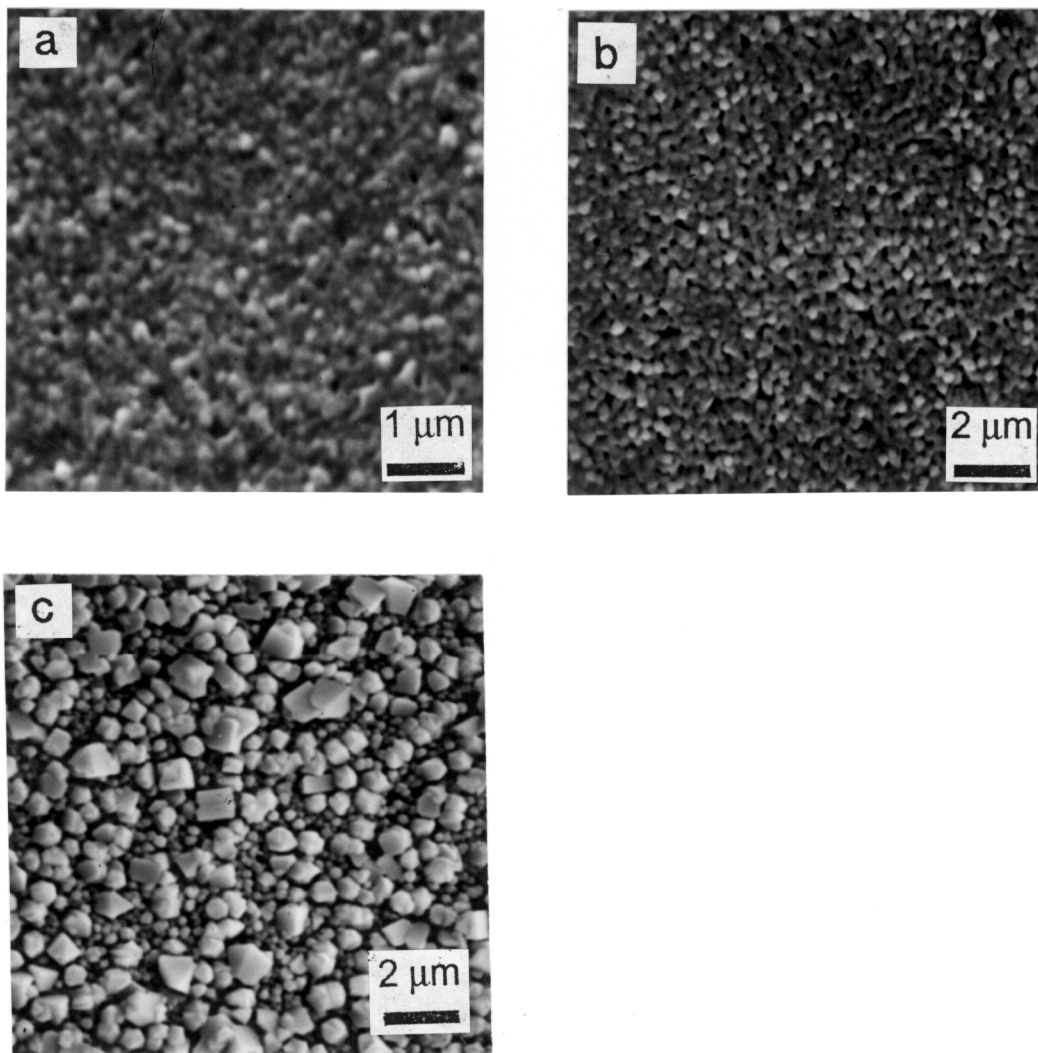


Figure 2.5 SEM micrographs of as-deposited MOCVD RuO_2 film on (a) quartz, and (b) Si (c) SiO_2/Si substrates.

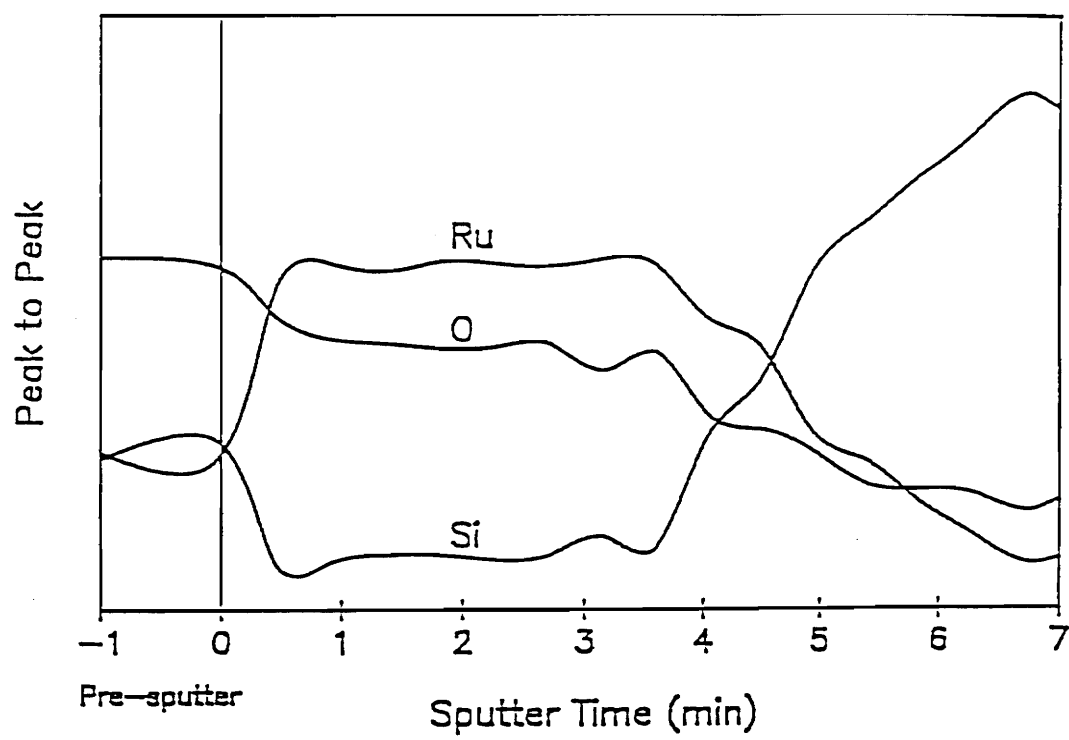


Figure 2.6 Auger depth profile of as-deposited MOCVD RuO₂ film on Si.

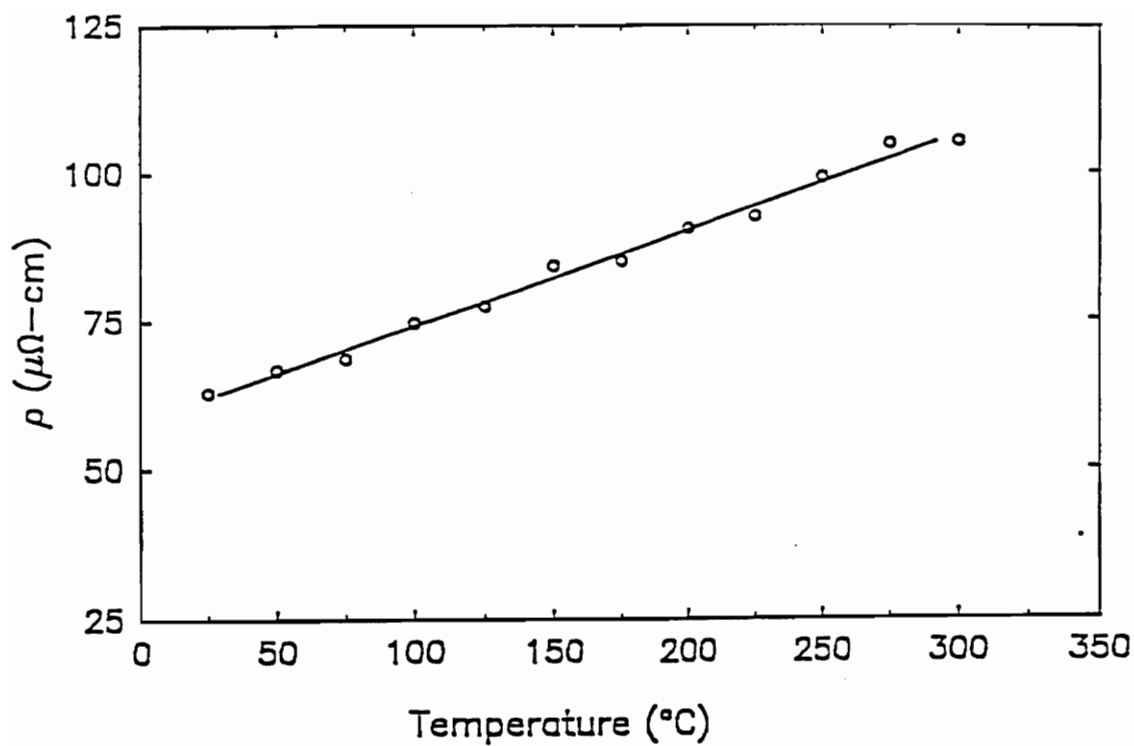


Figure 2.7 Resistivity of MOCVD RuO_2 film on quartz as a function of temperature.

resistivity as a function of annealing temperature had also been measured, as shown in Fig. 2.8. The resistivity decreased slightly upon annealing at 600°C and then increased with increasing annealing temperature. The resistivity ($60\ \mu\Omega\text{-cm}$) of the MOCVD RuO_2 film is lower than that of the reported MOCVD RuO_2 ($89\ \mu\Omega\text{-cm}$) [5], however, it is higher than that of the RF-sputtered RuO_2 film ($40\ \mu\Omega\text{-cm}$) [3]. It is still very promising for application in VLSI as a contact to a device.

The UV-VIS-NIR specular reflective spectrum of the RuO_2 film on fused quartz substrate is shown in Fig. 2.9. The reflectance of the spectrum increased with increasing wavelength in the NIR region and reached 63% at 2000 nm. Both the increasing reflectance and its high value indicate that the film has metallic character. Similar reflectance spectra have been obtained for reactively sputtered ruthenium oxide films [9].

2.5 SUMMARY

Pure and conducting RuO_2 thin films were successfully fabricated at a low temperature (550°C) on Si, SiO_2/Si and quartz substrates by MOCVD technique. The process parameters have been optimized. Lower deposition rate and sufficient oxygen pressure favor the formation of RuO_2 phase. Furthermore, film structures were not only dependent on MOCVD process parameters but also on substrate material. The as-deposited films were dense, crack-free and well adhered on the substrates. The Auger electron spectroscopy depth profile showed good compositional uniformity across the bulk of the films. The MOCVD RuO_2 thin films exhibited a resistivity as low as $60\ \mu\Omega/\text{cm}$. In addition, reflectance of RuO_2 in

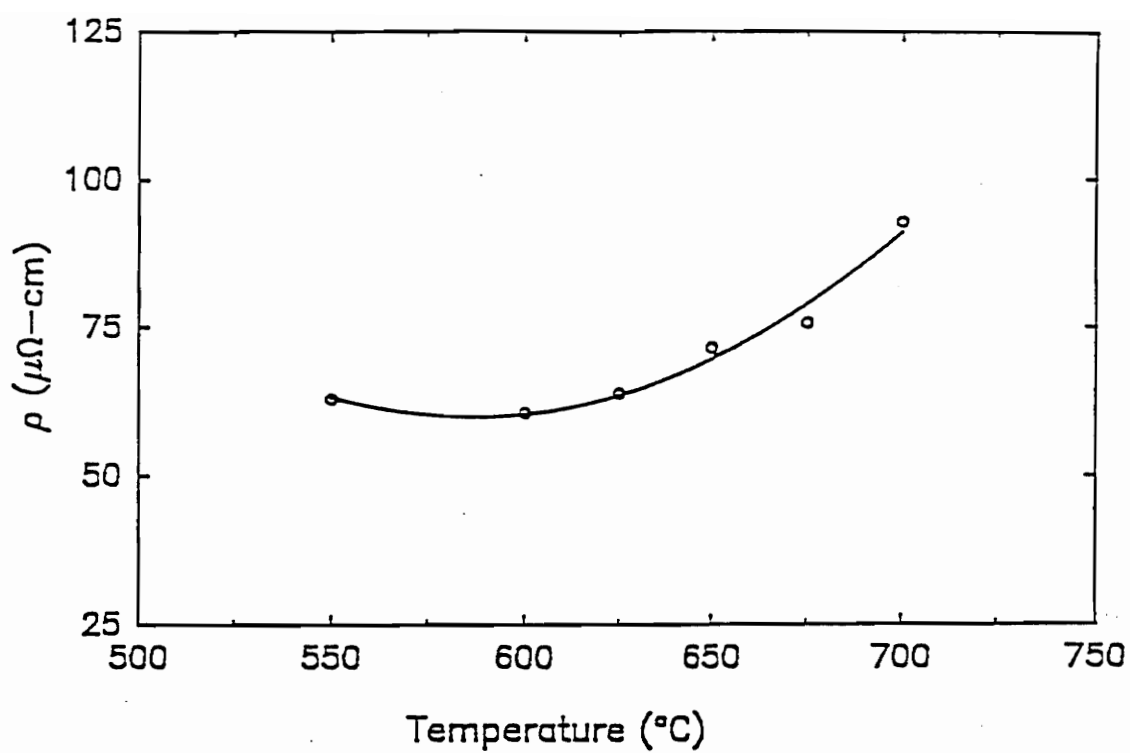


Figure 2.8 Resistivity of MOCVD RuO_2 film on quartz as a function of annealing temperature.

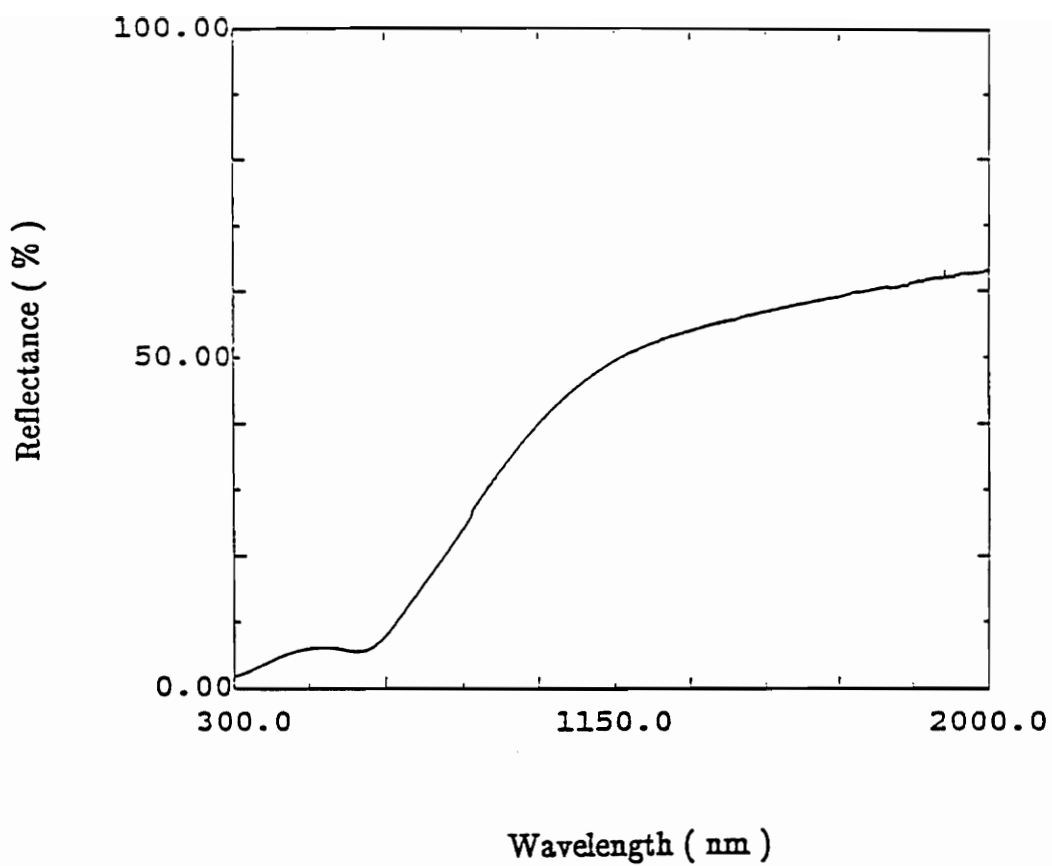


Figure 2.9 Specular reflectance spectrum of as-deposited MOCVD RuO_2 film on quartz.

the UV–VIS–NIR region had a metallic character.

ACKNOWLEDGEMENT

This study was partially supported by DARPA through a project from ONR. This work was also partially supported by Center for Advanced Ceramic Materials, the Virginia Center for Innovative Technology.

2.6 REFERENCES

1. A. T. Kuhn and C. J. Mortimer, "The Kinetics of Chlorine Evolution and Reduction on Titanium-Supported Metal Oxides Especially RuO_2 and IrO_2 ," J. Electrochem. Soc., 120, 231 (1973).
2. L. Krusin-Elbaum and M. Wittmer, "Conducting Transition Metal Oxides: Possibilities for RuO_2 in VLSI Metallization," J. Electrochem. Soc., 135(10), 2610 (1988).
3. L. Krusin-Elbaum, M. Wittmer, and D. S. Yee, "Characterization of Reactively Sputtered Ruthenium Dioxide for Very Large Scale Integrated Metallization," Appl. Phys. Lett., 50(26), 1879 (1987).
4. C. K. Kwok, D. P. Vijay, and S. B. Desu, "Conducting Oxide Electrodes for Ferroelectric Films," Proceedings of the 4th International Symposium on Integrated Ferroelectrics, Monterey, CA, 1992, (in press).
5. M. L. Green, M. E. Gross, L. E. Papa, K. J. Schnoes, and D. Brasen, "Chemical Vapor Deposition of Ruthenium and Ruthenium Dioxide Films," J. Electrochem. Soc., 132(11), 2677 (1985).
6. Q. X. Jia, and W. A. Anderson, "Sputter Deposition of $\text{YBa}_2\text{Cu}_3\text{O}_{7-x}$ Films on Si at 500°C with Conducting Metallic Oxide as a Buffer Layer," Appl. Phys. Lett., 57(3), 304 (1990).

7. Q. X. Jia, Z. Q. Shi, K. L. Jiao and W. A. Anderson, "Reactively Sputtered RuO₂ Thin Film Resistor with Near Zero Temperature Coefficient of Resistance," Thin Solid Films, 196, 29 (1991).
8. E. Kolawa, F. C. T. So, W. Flick, X. -A. Zhao, E. T-S. Pan and M-A. Nicolet, "Reactive Sputtering of RuO₂ Films," Thin Solid Films, 173, 217 (1989).
9. A. Belking, Z. Orban, and J. L. Vossen, "Optical Properties of RuO₂ Films Deposited by Reactive Sputtering," Thin Solid Films, 207, 242 (1992).

This paper entitled

**METALORGANIC CHEMICAL VAPOR DEPOSITION OF
ZrO₂ FILMS USING Zr(thd)₄ AS PRECURSORS**

was submitted to

JOURNAL OF MATERIALS RESEARCH

CHAPTER 3 METALORGANIC CHEMICAL VAPOR DEPOSITION OF ZrO_2 FILMS USING $\text{Zr}(\text{thd})_4$ AS PRECURSORS

3.1 ABSTRACT

Synthesis of zirconium tetramethylheptanedione [$\text{Zr}(\text{thd})_4$] was optimized. Purity of $\text{Zr}(\text{thd})_4$ was confirmed by melting point determination, carbon and hydrogen elemental analysis and proton nuclear magnetic resonance spectrometer (NMR). By using $\text{Zr}(\text{thd})_4$, excellent quality ZrO_2 thin films were successfully deposited on single crystal silicon wafers by metalorganic chemical vapor deposition (MOCVD) at reduced pressures. For substrate temperatures below 530°C , the film deposition rates were very small (≤ 1 nm/min). The film deposition rates were significantly affected by: (1) source temperature, (2) substrate temperature, and (3) total pressure. As-deposited films are carbon free. Furthermore, only the tetragonal ZrO_2 phase was identified in as-deposited films. The tetragonal phase transformed progressively into the monoclinic phase as the films were subjected to a high temperature post-deposition annealing. The optical properties of the ZrO_2 thin films as a function of wavelength, in the range of 200 nm to 2000 nm, were also reported. In addition, a simplified theoretical model which considers only a surface reaction was used to analyze the deposition of ZrO_2 films. The model predicted the

deposition rates well for various conditions in the hot wall reactor.

3.2 INTRODUCTION

ZrO₂ thin films, due to their variety of applications, are of considerable interest. For example, ZrO₂ films were utilized as thermal barrier coatings, as buffer layers for the growth of high T_c superconducting thin films, and as an active layer in high-temperature optical filters. Many different methods, such as reactive electron beam evaporation [1], dc and rf magnetron sputtering [2], and chemical vapor deposition (CVD) [3], have been employed for the fabrication of ZrO₂ thin films. Among these techniques, CVD seems to be a very promising and compatible method for electronic and optical device applications. The primary issue of CVD ZrO₂ thin films is the identification of a good precursor. ZrCl₄, which was first used as a precursor for CVD ZrO₂, requires very high deposition temperatures (> 800°C) and could result in the formation of fine powders [4]. The organometallic alkoxides such as zirconium i-propoxide, Zr(OPrⁱ)₄, and zirconium t-butoxide, Zr(OBu^t)₄, are also not suitable as precursors due to their instabilities [4]. However, zirconium acetylacetonates appear to be most suitable precursors for ZrO₂ deposition. Use of zirconium trifluoroacetylacetonate, Zr(C₅H₄F₃O₂)₄, for MOCVD of ZrO₂ films was reported earlier by our research group [4]. Although good quality ZrO₂ films were obtained using zirconium trifluoroacetylacetonate, the process parameter space is limited due to the possible fluorine contamination. Here we report on the synthesis and application of an acetylacetonate without fluorine, namely, [Zr(thd)₄] for the deposition of high quality ZrO₂ films. The Zr(thd)₄ synthesis was based on a method reported by Pinnavaia et al. [5], however, the method was optimized in our

study.

3.3 EXPERIMENTAL PROCEDURE

3.3.1 Synthesis of $\text{Zr}(\text{thd})_4$

The reactants for the $\text{Zr}(\text{thd})_4$ synthesis, zirconium tetrakis-acetylacetonate [$\text{Zr}(\text{acac})_4$] and tetramethylheptadione [H-thd], were initially purified. The recrystallized $\text{Zr}(\text{acac})_4$ (4.75g., 9.89 mmol) and distilled H-thd (28 ml, 136 mmol) were combined in a 100 ml round bottom flask which was equipped with a distilling head and distillate trap. The flask was immersed in an oil bath at 120°C . The apparatus was purged with dry nitrogen at a constant rate (100–150 ml/min) (Fig. 3.1), and approximately 7ml H-acac and H-thd was collected in the distillate trap. The constant stream of nitrogen through the apparatus helped the removal of H-acac and H-thd from the reaction flask. Therefore, the reaction was carried out at 120°C for 12 hours, instead of 145°C for 24 hours, as reported by Pinnavaia et al [5]. The flask containing $\text{Zr}(\text{thd})_4$ product and remaining H-acac and H-thd is equipped with a second distillation head and a cold trap. Freeze-thaw pump cycles under 0.004–0.01 torr are implemented to degas the excess ligand in the product mixture. During the thaw cycles, the product mixture was heated to 60 – 65°C to ensure the H-thd melted, and degassing took place. A liquid nitrogen bath was then placed at the distillate trap, and H-acac and H-thd was removed under continuous vacuum, with the product mixture at 65°C . Next, the product was recrystallized from toluene 3–4 times, or until any yellow color disappeared. Finally, the product was heated at 50°C in vacuum to remove any excess ligand and

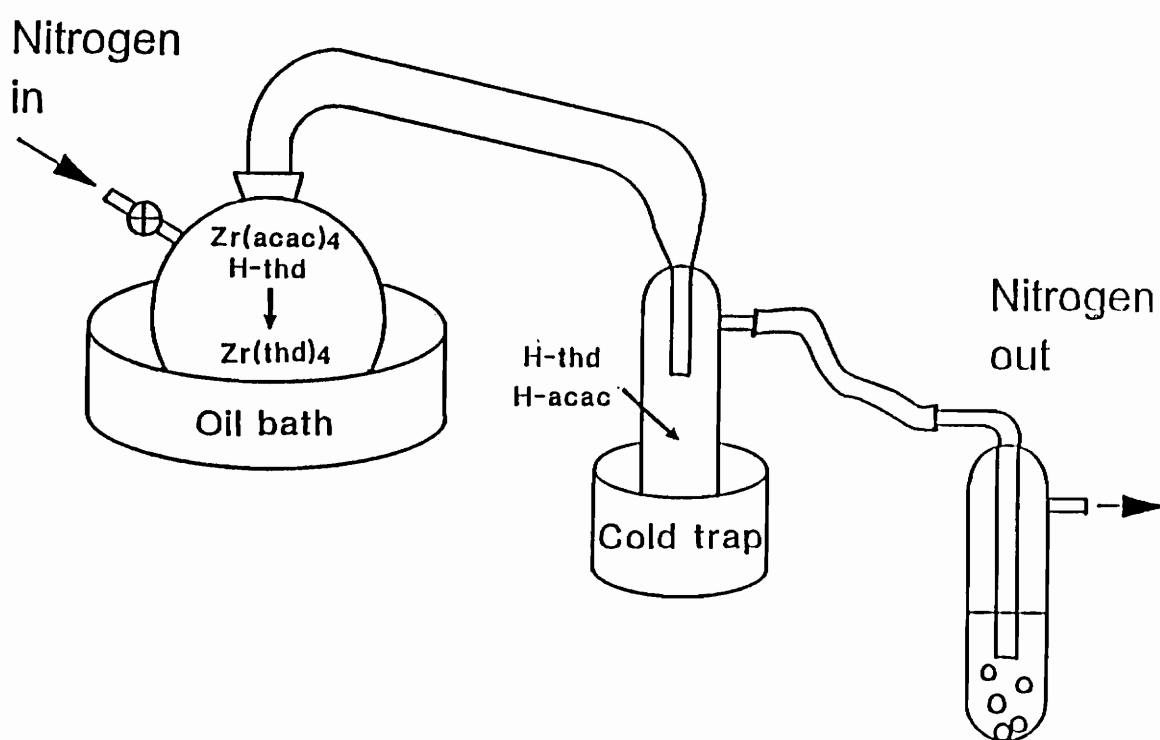


Figure 3.1 $\text{Zr}(\text{thd})_4$ synthesis apparatus.

solvent.

3.3.2 MOCVD and characterization of ZrO_2 films

ZrO_2 thin films were deposited in a reactor which was described in a previous paper [4]. Depositions were carried out at reduced pressures (4 to 10 torr). $\text{Zr}(\text{thd})_4$ was used as the precursor and the precursor temperature was varied from 230 to 240°C. The substrate temperature was also varied from 540 to 575°C. The precursor was carried by oxygen carrier gas into the reaction chamber. The film thicknesses were measured at the center of the silicon wafer by an ellipsometer at a wavelength of 632.8 nm. The films were also characterized by scanning electron microscopy (SEM) and electron spectroscopy for chemical analysis (ESCA) for surface morphology and carbon contamination, respectively. X-ray diffraction was used for phase identification. Optical transmission spectra of the films in the range of 200 nm to 2000 nm were obtained by an UV–VIS–NIR spectrophotometer.

3.4 RESULTS AND DISCUSSION

3.4.1 $\text{Zr}(\text{thd})_4$ synthesis

Following modifications were made to the reported synthesis process. By appropriately purifying the reactants and using nitrogen stream, both the temperature of the experiment and reaction time were decreased. Therefore, thermal decomposition of the reactants during the course of the procedure, which occurs due to excessive heating, and due to the use of impure reagents, was minimized. The

Zr(thd)₄ synthesized was a white crystalline product with a melting point of 345°C, which agrees with the melting point reported by Pinnavaia et al. [5]. The absence of any excess, nonbonded ligand was confirmed by proton nuclear magnetic resonance spectroscopy [6]. Carbon and hydrogen elemental analyses of the compound were: 63.95% carbon, 9.15 % hydrogen, which compare well with the calculated values: 64.16% carbon, 9.23 % hydrogen [6].

3.4.2 MOCVD of ZrO₂ films

The isothermal gravimetric (TGA) experiments of Zr(thd)₄ were carried out in the temperature range from 180°C to 260°C [6]. Zr(thd)₄ is thermally stable over the range of vaporization temperatures of the TGA, and the vaporization rate increased with increasing vaporization temperature. The calculated vapor pressures of Zr(thd)₄ range from approximately 1–100 millitorr [Fig. 3.2] [6]. Therefore, source temperatures in the range of 230 to 240°C were used for this study. The amount of source materials transported to the reactor was controlled by adjusting the source temperature and/or the carrier gas flow rate. In the range of experimental parameters investigated, source temperature, substrate temperature, and total pressure, were found to have significant effects on the film deposition rate. Fig. 3.3 shows the variation of the deposition rate with the substrate temperature at source temperatures of 230°C and 240°C, and at a pressure of 6 torr. The deposition rate increased with increasing substrate temperature and source temperature. It was also found that the deposition rate increased with increasing total pressure, as can be seen in Fig. 3.4. Therefore, the deposition rate of ZrO₂ thin films using Zr(thd)₄ can be easily controlled (from 6 to 18 nm/min) by adjusting the above

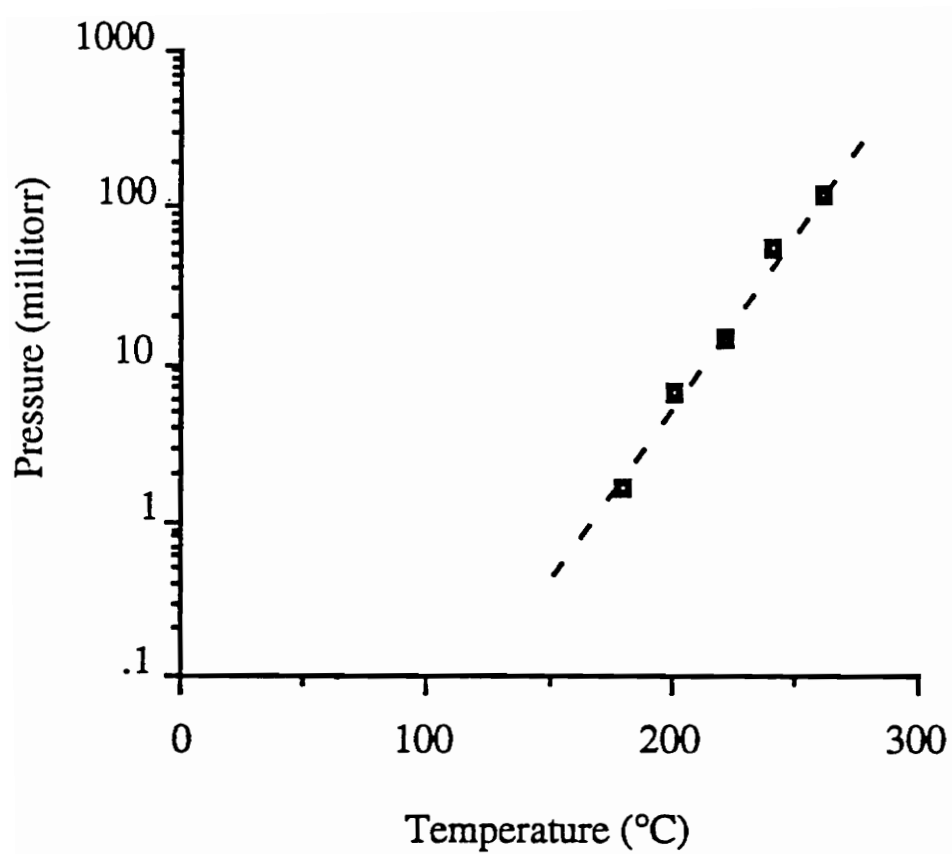


Figure 3.2 Vapor pressure of $\text{Zr}(\text{thd})_4$ as a function of temperature [6].

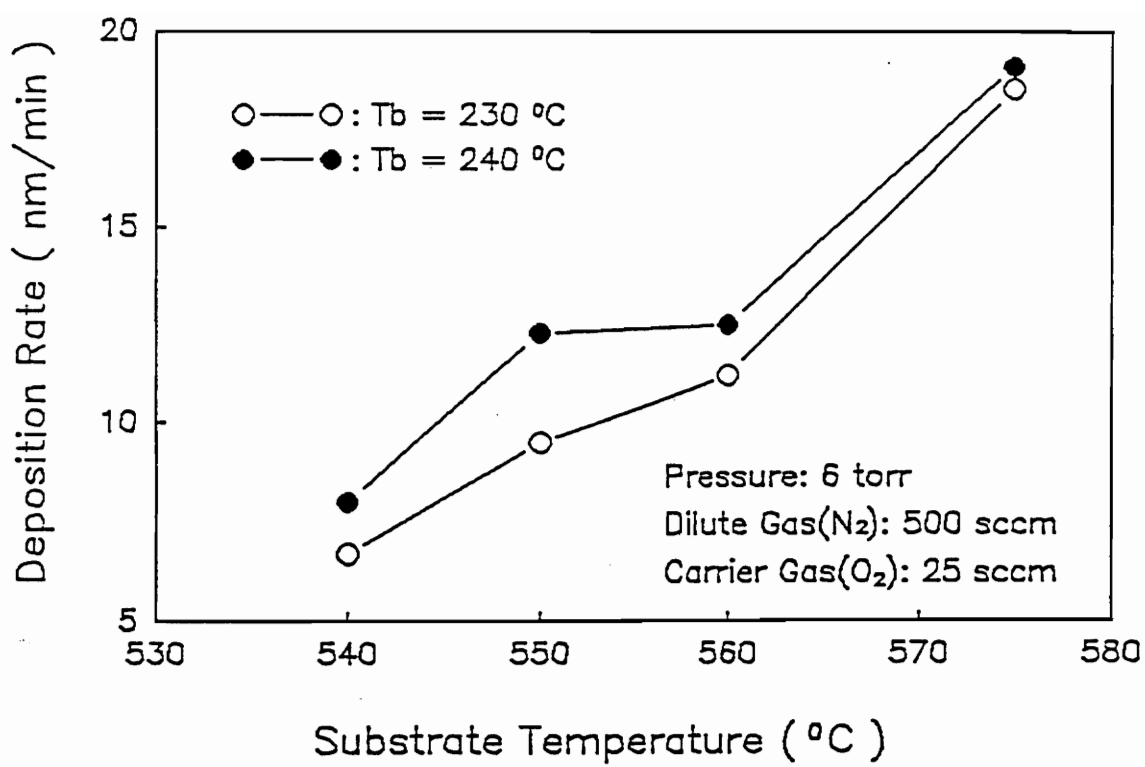


Figure 3.3 Deposition rate as functions of substrate and source temperature.

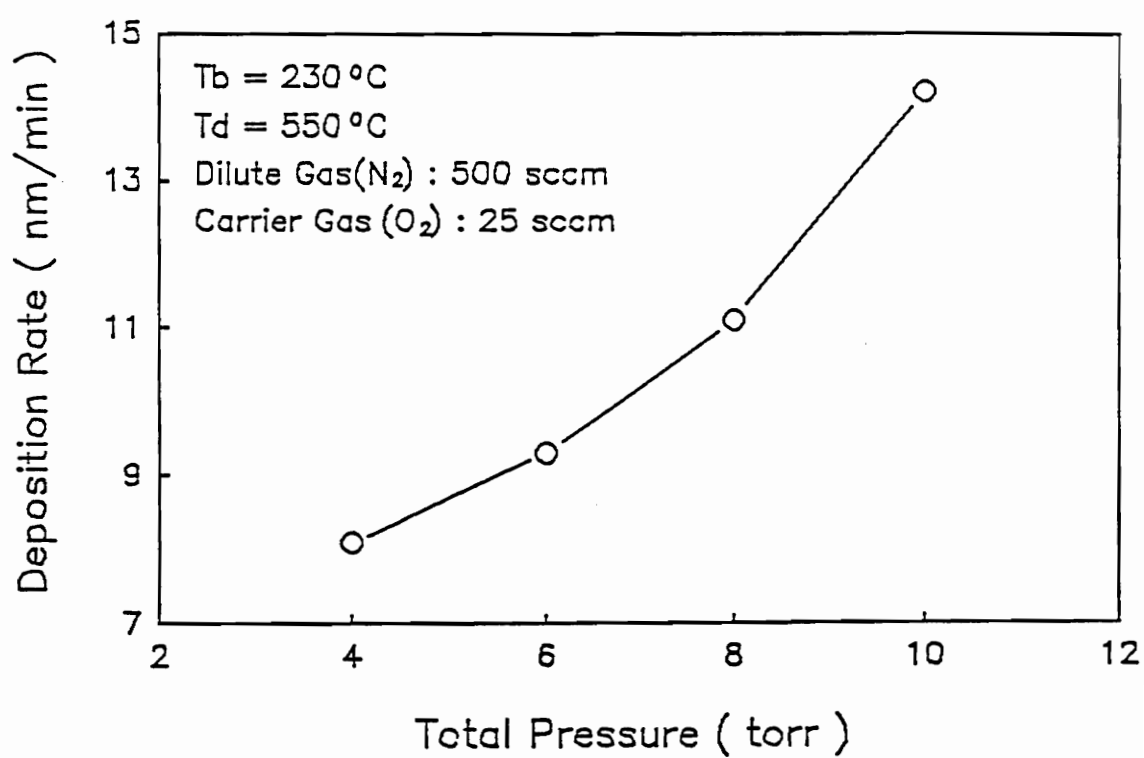


Figure 3.4 Deposition rate as a function of total pressure.

parameters.

3.4.3 Characterization of ZrO₂ film

As-deposited MOCVD ZrO₂ thin films were specular, crack-free, and adhered well to the substrates. Fig. 3.5 shows the surface morphology of the MOCVD ZrO₂ film which was annealed at 1000°C for one hour. The average grain size was estimated to be around 100 nm in this annealed sample.

The ESCA spectra of the film before and after five minutes of argon sputtering are illustrated in Fig. 3.6. The carbon peak in Fig. 3.6(a) was due to carbon adsorption on the sample surface. After five minutes of ion sputtering, only Zr and O peaks were observed [Fig. 3.6(b)]. This indicates that the carbon content of the film is below the ESCA detectable limit.

Fig. 3.7 displays the X-ray diffraction patterns for the ZrO₂ thin film as a function of post-deposition annealing temperature. Only the tetragonal phase was identified in the as-deposited thin film, while the formation of the monoclinic phase was noted in the sample which was annealed at 600°C. After the sample was subjected to a high temperature (1000°C) heat treatment, it was found that the monoclinic phase was the major phase in the thin film.

The FTIR absorption spectra of the same samples as a function of annealing temperature were shown in Fig. 3.8. The six prominent absorption peaks of the post-deposition annealed samples agreed very well with that of the CVD monoclinic

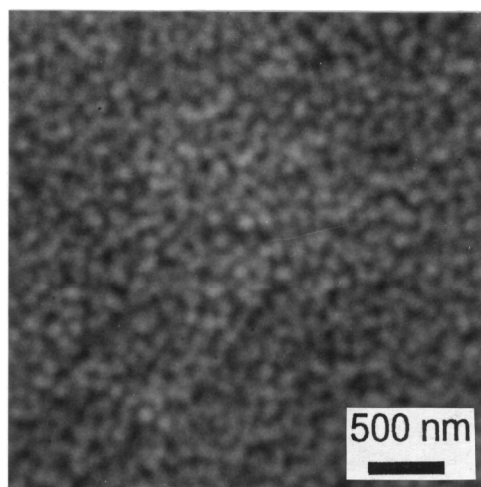


Figure 3.5 SEM micrograph of 1000°C annealed ZrO₂ film on Si substrate.

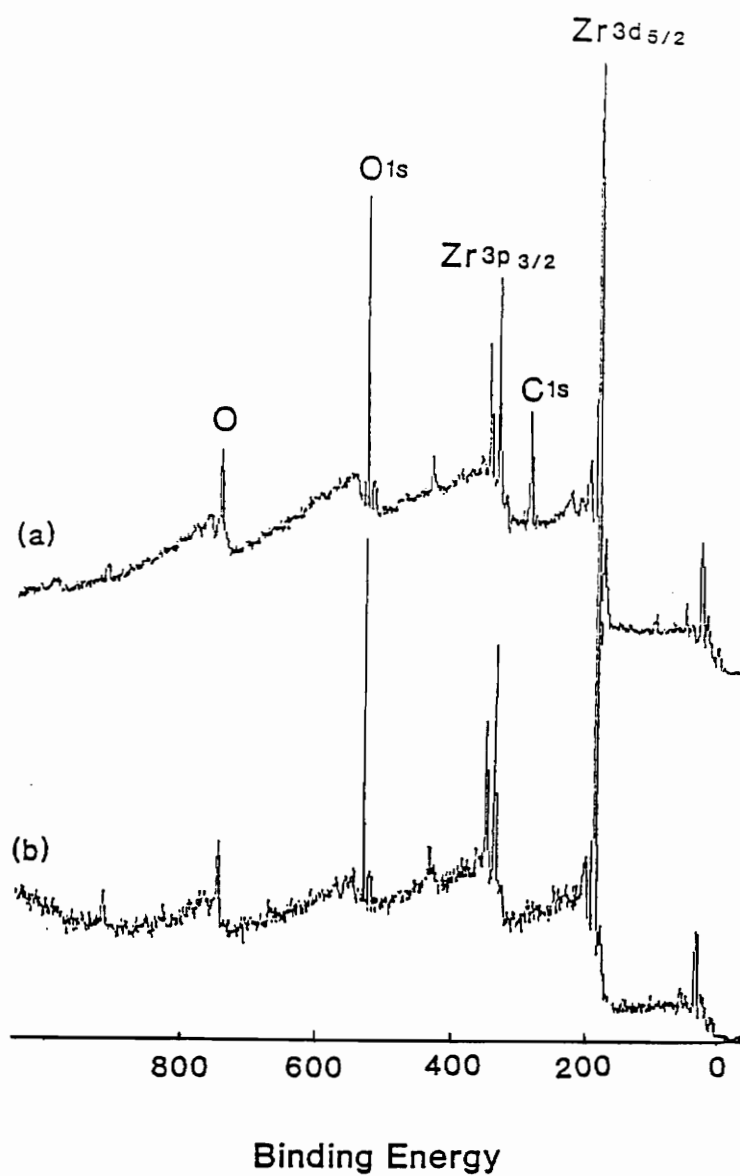


Figure 3.6 ESCA spectra of ZrO_2 film (a) before sputtering, (b) after sputtering.

T: Tetragonal
M: Monoclinic

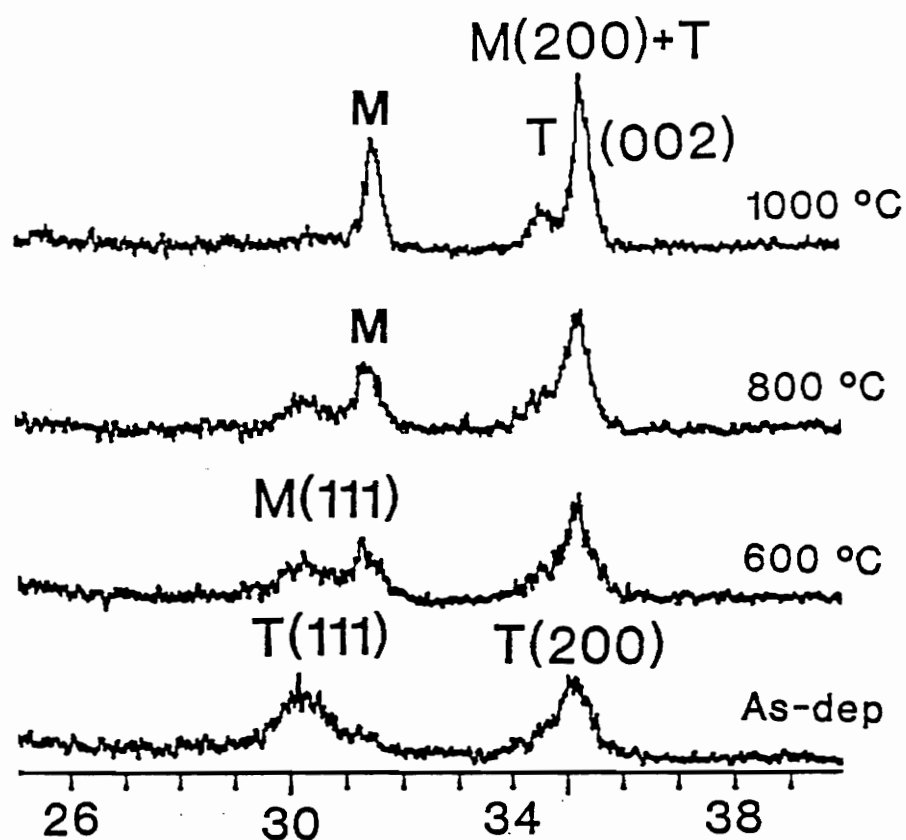


Figure 3.7 X-ray Diffraction pattern of MOCVD ZrO₂ film.

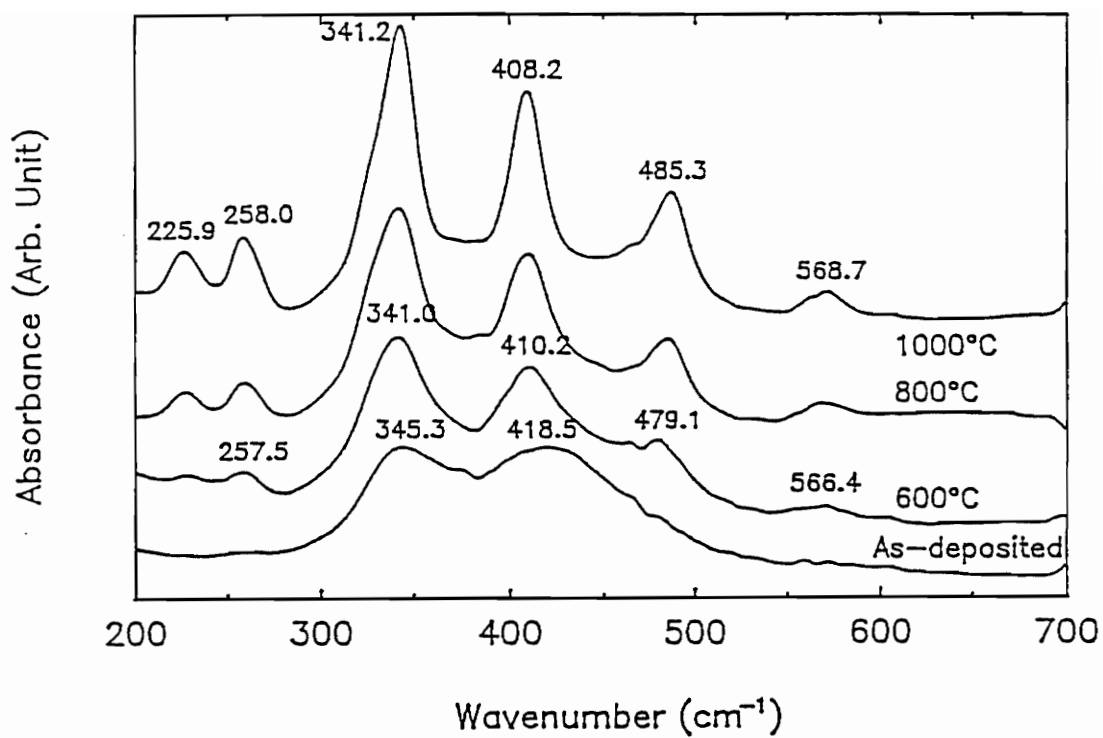


Figure 3.8 FTIR spectra of MOCVD ZrO₂ film.

ZrO₂ thin films obtained by Tauber [3]. Since the as-deposited film consisted of only tetragonal phase according to X-ray diffraction result, we attribute the two absorption peaks in the FTIR spectrum (Fig. 3.8) of as-deposited sample to the lattice vibration modes of the tetragonal phase. However, the absorption peaks of tetragonal phase could not be identified in the spectra of the annealed samples, which may be due to the overlap with the major peaks of the monoclinic phase.

There is a large scatter in the reported data about the phases existing in ZrO₂ thin film [1,3,7]. However, there is a general agreement that the number and nature of the phases in the film are a sensitive function of the deposition process, grain size, and thickness [8]. In our study, the formation of the metastable tetragonal phase at the deposition temperature (e.g. 550°C) may be related to the high deposition rate, film stress, and/or to the fine grain size. When the films were subjected to high-temperature heat treatments, the thermodynamically favored monoclinic phase formed gradually.

The UV-VIS-NIR transmission spectra of the as-deposited and annealed MOCVD ZrO₂ thin films on fused quartz substrates are shown in Fig. 3.9. As can be seen from Fig. 3.9, the transmittance drops down to 0% at $\lambda = 207$ nm (the absorption edge), while its value is around 90% in the visible and near infrared range. An envelope method [9] was used to calculate the refractive index (n) and the thickness of the film. The thickness of the film was calculated to be 370 nm. Fig. 3.10 shows the refractive index of the as-deposited and annealed ZrO₂ films as a function of wavelength. The indices of refraction increased with the increasing annealing temperature. The change of the refractive index upon annealing can be

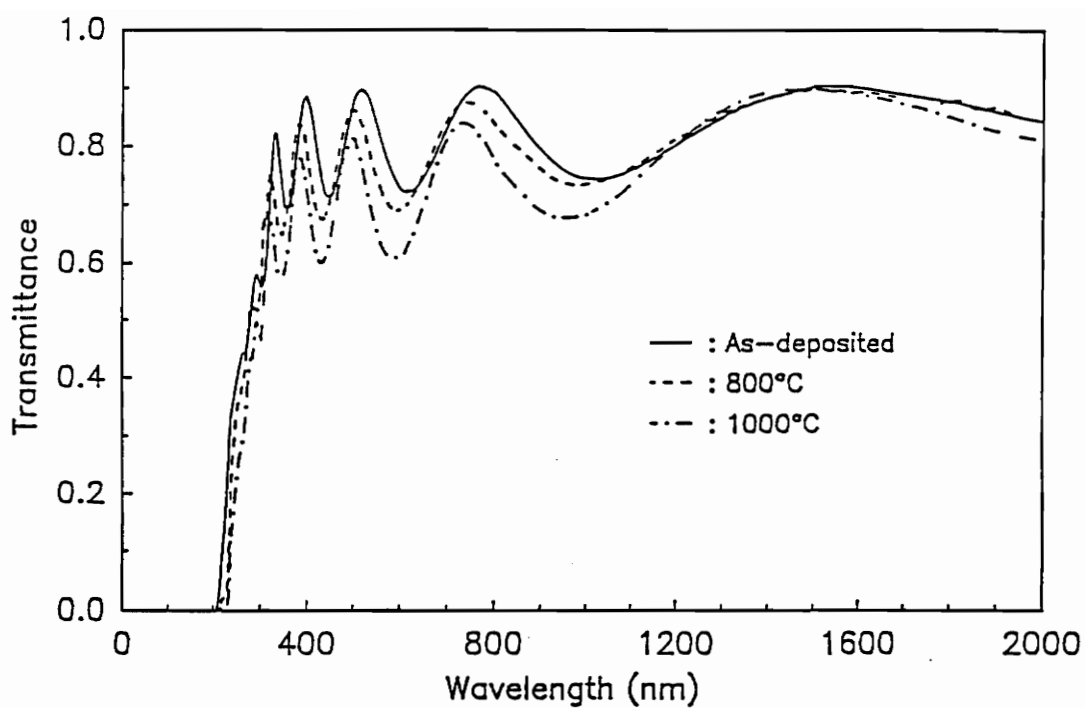


Figure 3.9 Specular transmission spectra of the MOCVD ZrO_2 film on fused quartz.

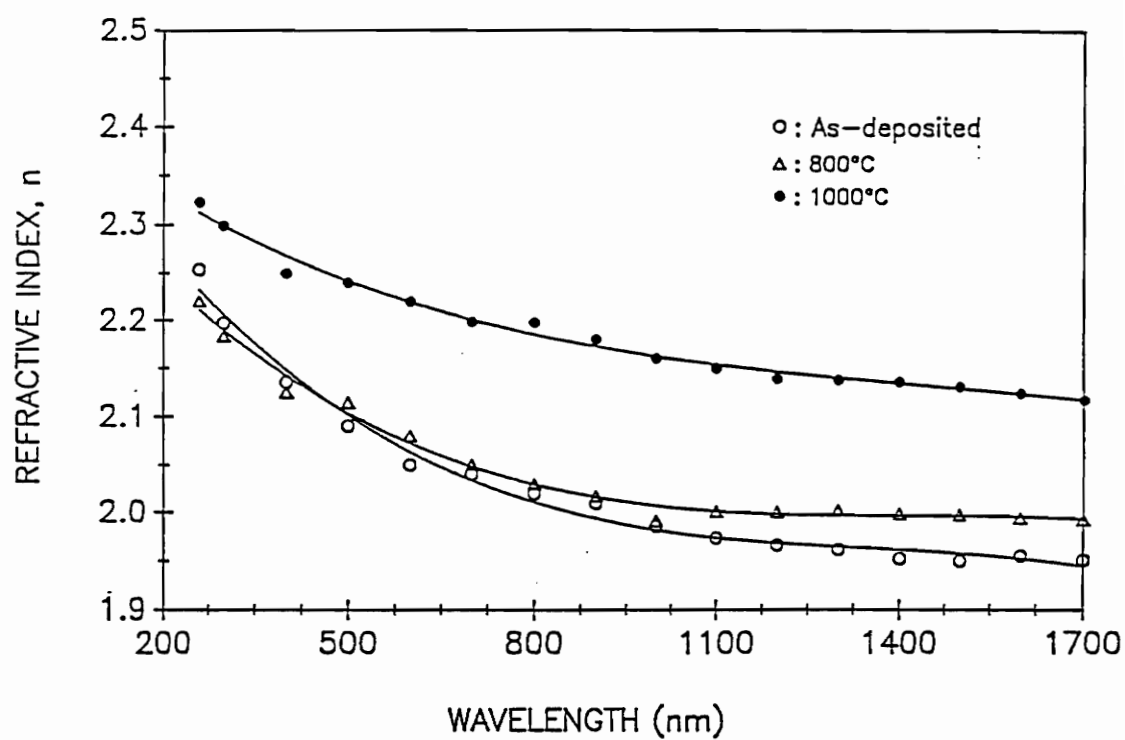


Figure 3.10 Variation of refractive index with wavelength.

attributed to the phase transformations of the films.

3.4.4 Kinetic Study of Hot–Wall MOCVD ZrO_2

The measured temperature profiles of the hot–wall CVD reactor is shown in Fig. 3.11 with the setting points being equal to 540°C , 550°C , and 560°C . As can be seen, a uniform temperature ($\pm 5^\circ\text{C}$) zone of 300 mm long is located around the the center of the CVD reactor.

Deposition rates of ZrO_2 film, measured at the substrates located 25 cm, 40 cm and 55 cm away from the entrance (as shown in Fig. 3.11), versus deposition temperatures for two bubbler setting temperatures are shown in Figs. 3.12a, b and c.

As shown in Figs. 3.11 and 3.12a, the effective activation energy of the ZrO_2 CVD process was found to be 73.4 kJ/mol if the deposition rates were measured at the 1 location. The effective activation energy changes to 66.6 kJ/mol and 97.4 kJ/mol if the deposition rates were measured at the 2 and 3 locations. For all cases, the effective activation energies are independent of the bubbler setting temperature, as shown in Figs. 3.12(a–c). Changes of the effective activation energy can be attributed to the depletion of $\text{Zr}(\text{thd})_4$ precursors from Zone A to Zone C, as shown in Fig. 3.11. In order to avoid the undesirable spatial dependence of the effective activation energy, the mass transport, including both diffusion and convection, has to be considered in analyzing the deposition rates of the hot–wall CVD process.

Because detailed studies of the ZrO_2 film deposited from the $\text{Zr}(\text{thd})_4$

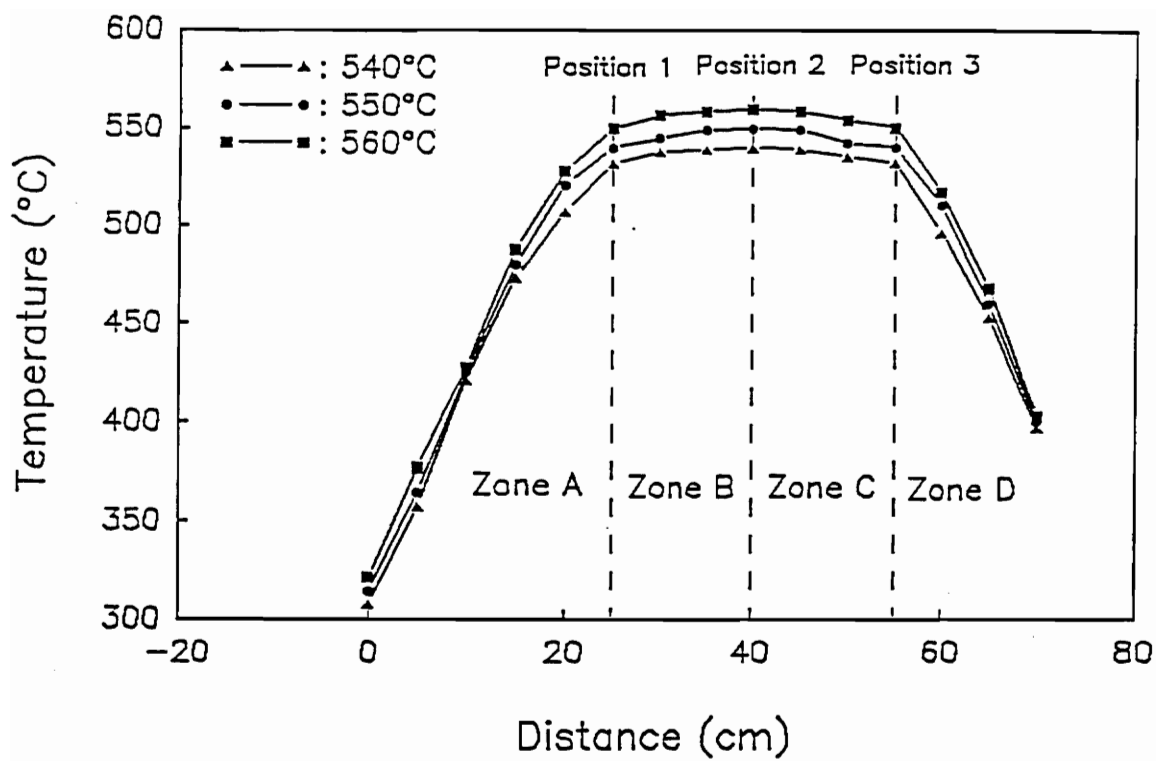


Figure 3.11 The measured temperature profiles of the MOCVD reactor.

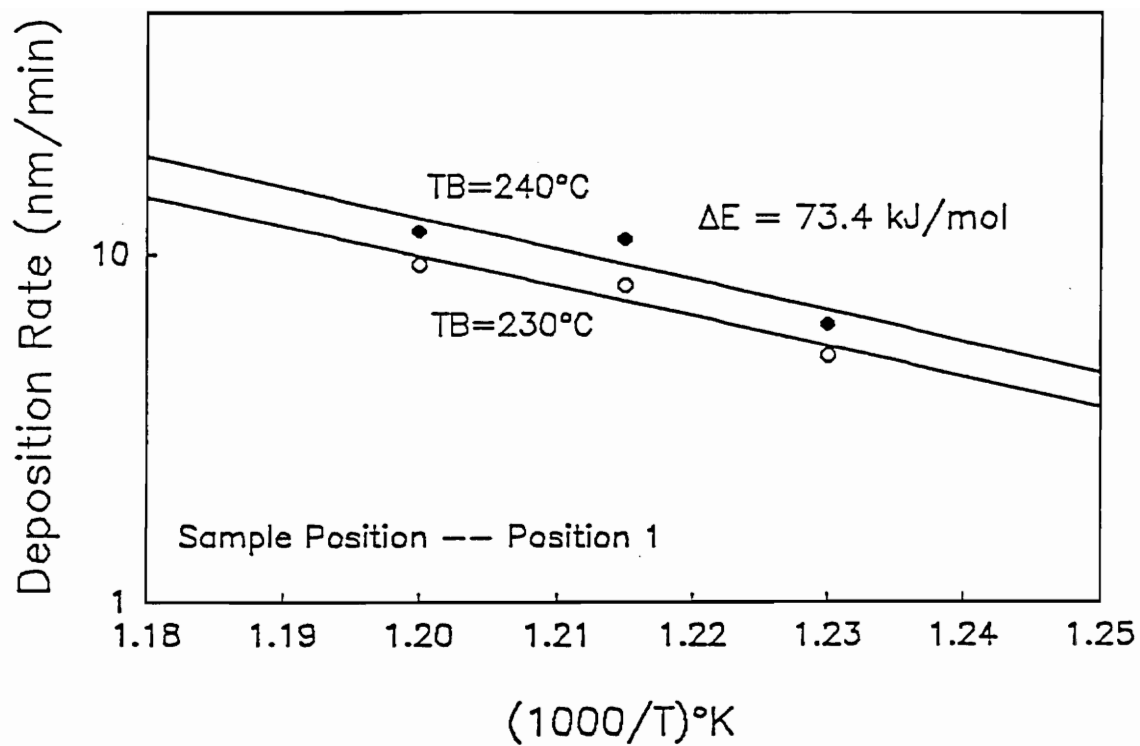


Figure 3.12(a) Deposition rates of ZrO_2 film versus deposition temperatures at position 1.

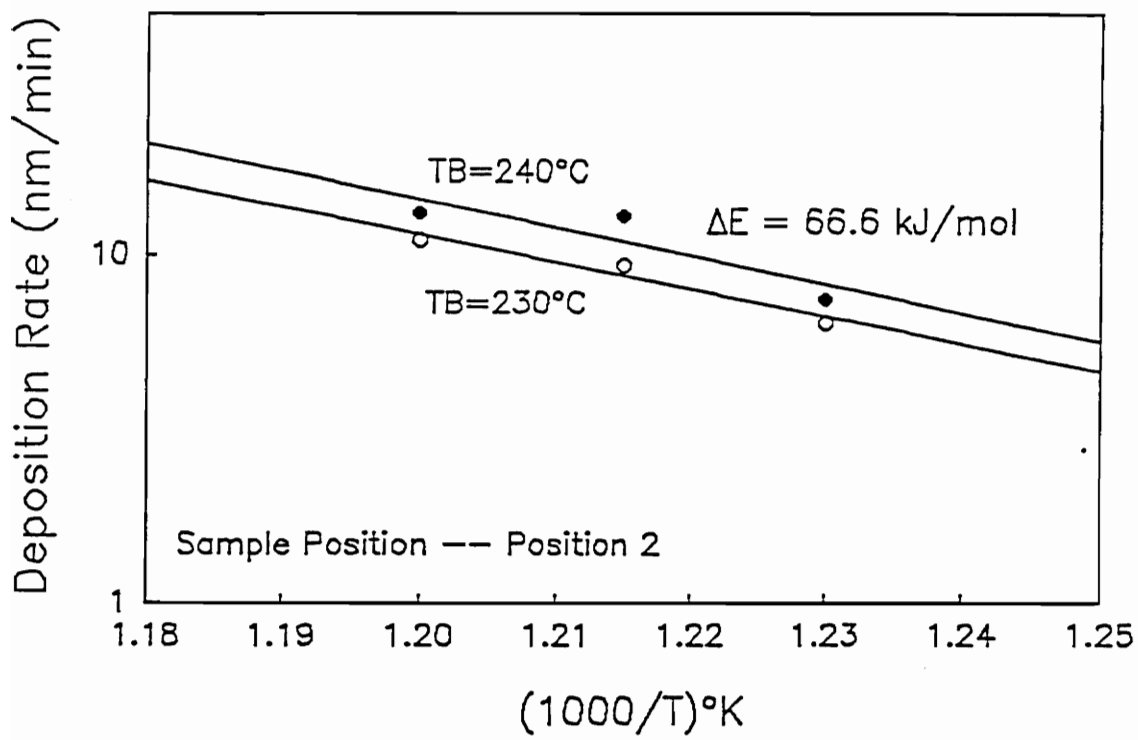


Figure 3.12(b) Deposition rates of ZrO_2 film versus deposition temperatures at position 2.

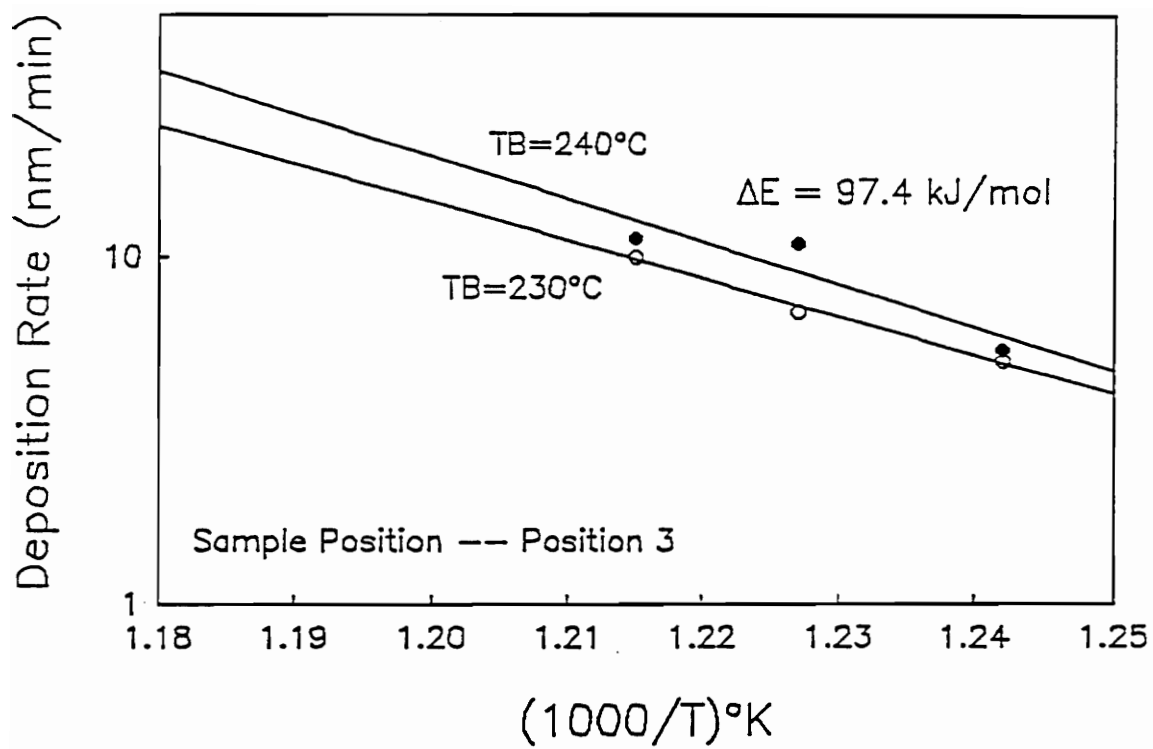
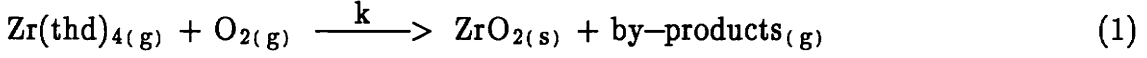


Figure 3.12(c) Deposition rates of ZrO_2 film versus deposition temperatures at position 3.

precursors are still lacking, an overall heterogeneous reaction was used in this work as a first approximation:



It was assumed that the deposition rate has Arrhenius-type dependence on the deposition temperature and is first-order in Zr(thd)_4 concentration:

$$k \text{ (cm/sec)} = k_0 \exp(-E_a/RT) \quad (2)$$

In the present study, we confine ourselves to a steady state analysis in one dimension (1-D). As a result, the equation of continuity of the Zr(thd)_4 precursor can be expressed as [10–13]:

$$-D \frac{\partial^2 C}{\partial x^2} + U \frac{\partial C}{\partial x} = -kC \frac{A}{V} \quad (3)$$

where C is the concentration of Zr(thd)_4 in mol/cm^3 , D (cm^2/sec) is the diffusion coefficient of Zr(thd)_4 , U (cm/sec) is velocity of the gaseous mixture, x (cm) is the distance along the CVD reactor, and A/V (cm^{-1}) is the reaction area per unit volume of the CVD reactor.

The flow velocity U was assumed to be equal to Q/A , where Q is the entrance volume flow rate (cm^3/sec). The diffusion constant D is approximated as [14]:

$$1/D = 1/D_{\text{bulk}} + 1/D_{\text{knudsen}} \quad (4)$$

where D_{bulk} was assumed to be equal to $8000 \text{ cm}^2/\text{sec}$ at 1 Torr and 298°K , D_{knudsen} is equal to $9700 r(\text{cm}) \sqrt{[T(^{\circ}\text{K})/M]}$ [16], with r being the radius of the CVD reactor and M being the molecular weight of $\text{Zr}(\text{thd})_4$.

Because of the nonhomogeneous nature associated with the thermal profiles, an exact solution could not be obtained of the equation (3). The finite element method (FEM) was used to solve the equation (3) numerically. Two-node linear elements were used in this study. Details of the FEM can be found in references 12, 13, and 16.

The boundary conditions for the 1-D mass transport equation was assumed to be:

$$\text{At entrance:} \quad C = P/RT \quad (5A)$$

where P is the entrance pressure of $\text{Zr}(\text{thd})_4$ precursor. The pressure of $\text{Zr}(\text{thd})_4$ is equal to $12\text{e-}3$ and $14\text{e-}3$ Torr at 230°C and 240°C bubbler temperatures [17].

$$\text{At exit:} \quad dC/dx = 0 \quad (5B)$$

The reaction constant k was determined by matching the experimental results with the FEM calculations at various deposition temperatures. Results were shown in Figs 3.13(a,b). In the calculations, the ZrO_2 deposition rate was assumed to be [11]:

$$\text{ZrO}_2 \text{ Deposition Rate} = kC \frac{M_f}{\rho} \quad (6)$$

where M_f (mol/cm³) is the molecular weight of the ZrO₂ film, and ρ (g/cm³) is the density of the ZrO₂ film.

Agreements between the experimental results and modeling calculations were found to be good, as shown in Figs. 3.13(a,b). The reaction constant k was found to be:

$$k = 6.0 \times 10^4 \text{ nm/sec exp}(-175/(RT) \text{ kJ/mol}) \quad (7)$$

3.5 SUMMARY

Zr(thd)₄ was synthesized and synthesis process was optimized. Since Zr(thd)₄ is thermal stable and has acceptable vapor pressure, It was shown to be a very good precursor for depositing excellent quality MOCVD ZrO₂ thin films. As-deposited ZrO₂ thin films were fine-grained and stoichiometric. In addition, the deposition rate can be easily controlled from 6 to 18 nm/min by adjusting the deposition parameters in the range of experimental parameters investigated. Only the tetragonal phase was observed in the as-deposited films. The tetragonal phase transformed progressively into the monoclinic phase as the films were subjected to high-temperature post-deposition annealing. The FTIR spectra of both the tetragonal and monoclinic ZrO₂ thin film were obtained. The optical properties of the ZrO₂ thin films as a function of wavelength, in the range of 200 nm to 2000 nm, were obtained. In addition, a simplified theoretical model which considers only a

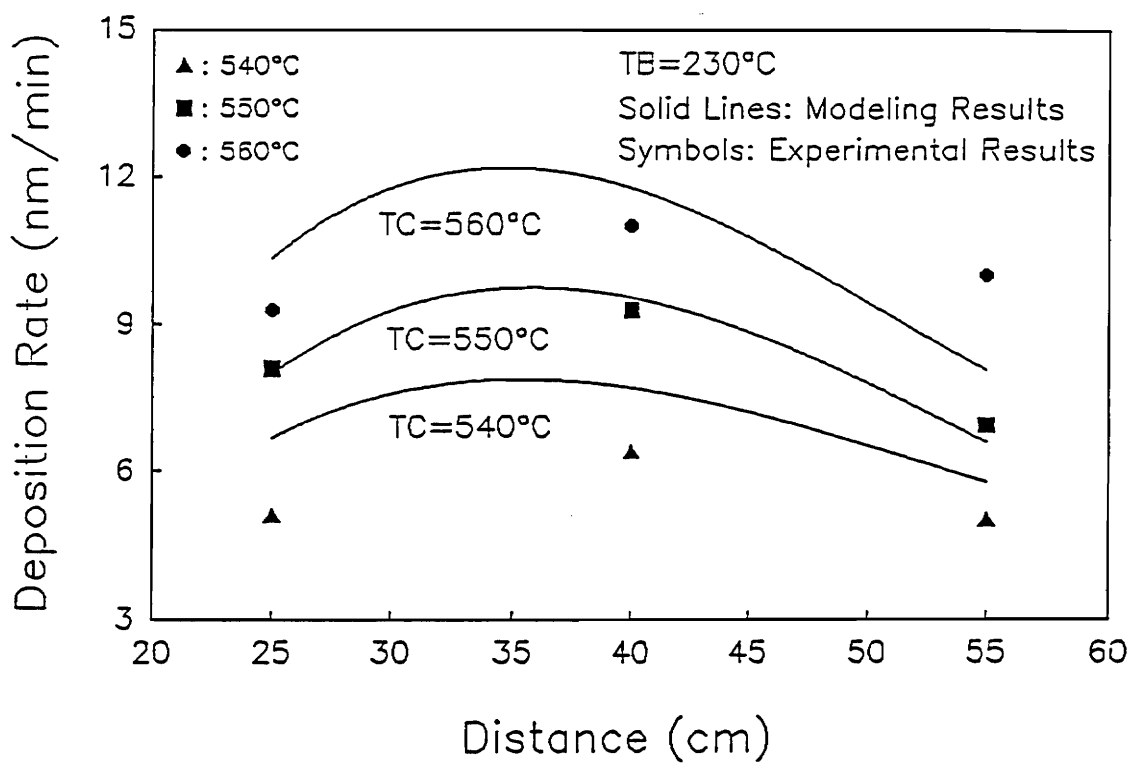


Figure 3.13(a) Comparison of the experimental results with the modeling data.

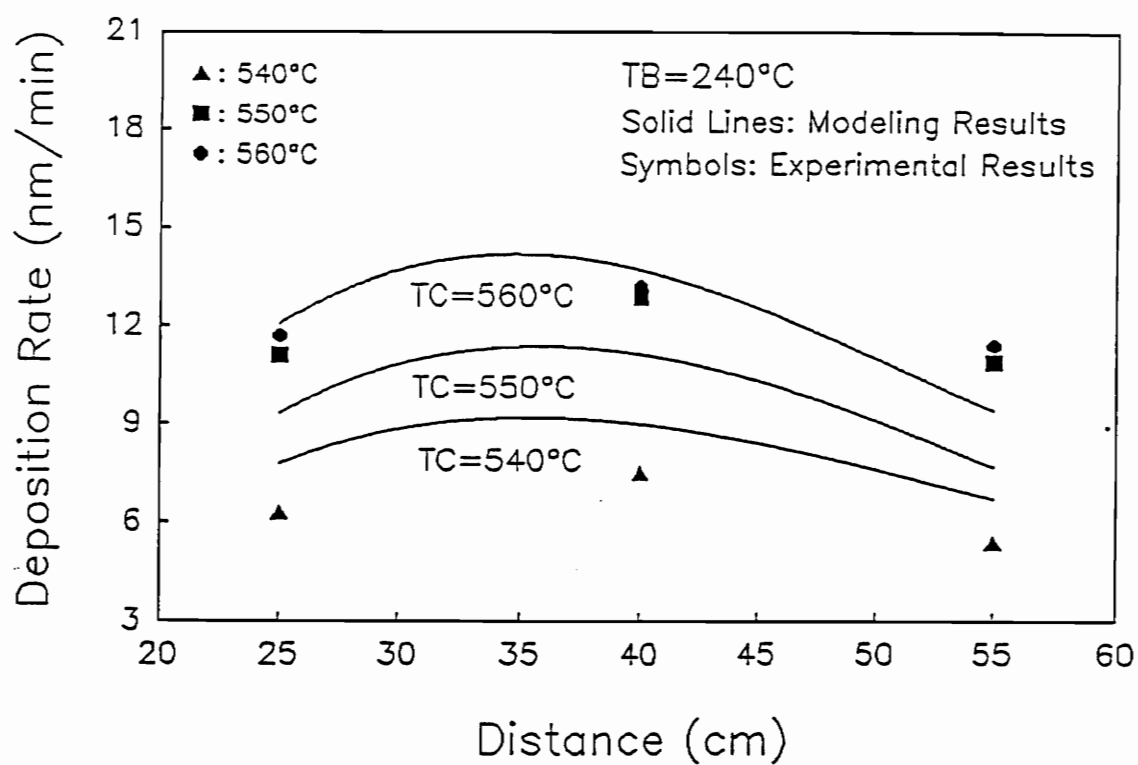


Figure 3.13(b) Comparison of the experimental results with the modeling data.

surface reaction was used to analyze the deposition of ZrO_2 film. The deposition rates were predicted well for various deposition conditions in the hot wall reactor with this model.

ACKNOWLEDGEMENT

We would like to thank May Nyman for her help in synthesizing the precursor. We wish to acknowledge the support of DARPA through a project from ONR to this study. This work was also partially supported by the Center for Advanced Ceramic Materials, the Virginia Center for Innovative Technology.

3.6 REFERENCES

1. M. Ghanashyam Krishna, K. Narasimha Rao, and S. Mohan, "Optical and Structural Characterization of Evaporated Zirconia Films," Appl. Phys. Lett., 57(6), 557 (1990).
2. C. Deshpandey and L. Holland in *Proceedings of the 7th International Conference on Vacuum metallurgy*, Iron Steel Institute of Japan, Tokyo, 1, 276 (1982).
3. R. N. Tauber, A. C. Dumbri, and R.E. Caffrey, "Preparation and Properties of Pyrolytic Zirconium Dioxide Films," J. Electrochem. Soc., 118, 747 (1971).
4. S. B. Desu, S. Tian, and C. K. Kwok, "Structure, Composition, and Properties of MOCVD ZrO_2 Thin Films," Mat. Res. Soc. Symp. Proc., 168, 349 (1990)
5. Thomas J. Pinnavaia, Michael T. Mocella, Bruce A. Averill, and John T. Woodward, "Redistribution Reactions of d^0 Metal Diketonates Containing MO_6 and MO_8 Cores," Inorganic Chemistry, 12(4), 763 (1973).
6. M. Nyman, "Synthesis and Characterization of Precursors for Chemical Vapor Deposition of Metal Oxide Thin Films," M. S. Thesis, Virginia polytechnic institute and state university, July 1992.
7. C. K. Kwok and C. R. Aita, "Near-band Gap Optical Behavior of Sputter Deposited α - and $\alpha+\beta$ - ZrO_2 Films," J. Appl. Phys., 66(6), 2756 (1989).

8. E. N. Farabaugh, A. Feldman, J. Sun, and Y. N. Sun, "Examination of Thin Films in the $\text{ZrO}_2\text{--SiO}_2$ System by Transmission Electron Microscopy and X-ray Diffraction Techniques," *J. Vac. Sci. Technol.*, A 5(4), 1671 (1987).
9. J. C. Manifacier, J. Gasiot, and J. P. Fillard, "A Simple Method for the Determination of the Optical Constants n,k and the Thickness of a Weakly Absorbing Thin Film," *J. Phys. E: Sci. Instrum.*, 9, 1002 (1976).
10. R.B. Bird, W.E. Steward, and E.N. Lightfoot, *Transport Phenomena*, (John Wiley & Sons, New York, 1960).
11. Seshu B. Desu and Surya R. Kalidindi, "Determination of Rate Controlling Step in CVD Processes with Gas Phase and Surface Reactions," *Jap. J. of Appl. Phys.*, 29, 1310 (1990)
12. C.Y. Tsai, Seshu B. Desu, Chien C. Chiu, and J.N. Reddy, "The Role of Gas-Phase Reaction in Modeling of the Forced-Flow Chemical Vapor Infiltration Process," *J. Electrochem. Soc.*, 140, 2121 (1993)
13. C.Y. Tsai and Seshu B. Desu, "Contribution of Gas-Phase Reactions to the Deposition of SiC by a Forced-Flow Chemical Vapor Infiltration Process," *Mater. Res. Soc. Symp.*, 250, 227 (1992)
14. R. Jackson, *Transport in Porous Catalysts*, (Elsevier North-Holland, New York, 1977).

15. E. L. Cussler, *Diffusion: Mass Transport in Fluid Systems*, (Cambridge University Press, New York, 1984).
16. J.N. Reddy, *An Introduction to the Finite Element Method*, (McGraw–Hill Book Company, New York, 1984).

This paper entitled

**FERROELECTRIC BISMUTH TITANATE FILMS BY HOT
WALL METALORGANIC CHEMICAL VAPOR
DEPOSITION**

was published in

JOURNAL OF APPLIED PHYSICS

CHAPTER 4 FERROELECTRIC BISMUTH TITANATE FILMS BY HOT WALL METALORGANIC CHEMICAL VAPOR DEPOSITION

4.1 ABSTRACT

Ferroelectric bismuth titanate thin films were deposited on Si, sapphire disks, and Pt/Ti/SiO₂/Si substrates by hot wall metalorganic chemical vapor deposition (MOCVD). Triphenyl bismuth [Bi(C₆H₅)₃] and titanium ethoxide [Ti(C₂H₅O)₄] were used as the precursors. The deposition rates were in the range of 3.9–12.5 nm/min. The Bi/Ti ratio was easily controlled by precursor temperature, carrier gas flow rate, and deposition temperature. As-deposited films were pure Bi₄Ti₃O₁₂ phase. The films were specular and showed uniform and fine grain size. Optical constants as a function of wavelength were calculated from the film transmission characteristics in the UV–VIS–NIR region. The 550°C annealed film showed a spontaneous polarization of 26.5 μC/cm² and a coercive field of 244.3 kV/cm.

4.2 INTRODUCTION

Bismuth titanate (Bi₄Ti₃O₁₂) is one of the few important ferroelectric materials. This compound has a high Curie temperature of 675°C. In a single

crystal, there are two polarization axes: the major one, with $P_s = 50 \mu\text{C}/\text{cm}^2$, along the a axis of the (pseudo-)orthorhombic structure, while the minor polarization axis, with $P_s = 4 \mu\text{C}/\text{cm}^2$, along the c axis. The coercive fields are 50 and 3–5 kV/cm for a and c axes, respectively [1]. $\text{Bi}_4\text{Ti}_3\text{O}_{12}$ also has a unique rotation of the optical indicatrix upon polarization switching [2]. These interesting properties have enabled a variety of applications. A ferroelectric field-effect memory device using $\text{Bi}_4\text{Ti}_3\text{O}_{12}$ thin film has been reported [3]. It has been also considered as an alternate ferroelectric material for ferroelectric random access memories (FRAMs) and dynamic random access memories (DRAMs). $\text{Bi}_4\text{Ti}_3\text{O}_{12}$ thin films formed on a superconducting $\text{Bi}_2\text{Sr}_2\text{CaCuO}_{6+x}$ bottom electrode showed promising ferroelectric properties, as well as good radiation hardness, excellent aging characteristics, and the potential for integration into semiconductor device processing technology [4]. In addition, modulator and display applications of $\text{Bi}_4\text{Ti}_3\text{O}_{12}$ have also been evaluated [2].

$\text{Bi}_4\text{Ti}_3\text{O}_{12}$ thin films have been prepared by rf sputtering [2], pulsed laser ablation [5,6], sol-gel processing [7], and metalorganic chemical vapor deposition (MOCVD) [8]. Among these techniques, MOCVD allows high deposition rate, excellent step coverage, and easy composition control, which are compatible with large scale processing. Miyajima et al reported MOCVD $\text{Bi}_4\text{Ti}_3\text{O}_{12}$ thin films on a heated substrate at 750°C by a cold wall type reactor [8]. To allow large scale processing and mass production, a low processing temperature and a hot wall type reactor are desirable. In this paper, we report on the structure and composition of the hot wall MOCVD $\text{Bi}_4\text{Ti}_3\text{O}_{12}$ thin films using $\text{Bi}(\text{C}_6\text{H}_5)_3$ and $\text{Ti}(\text{C}_2\text{H}_5\text{O})_4$ as precursors, as well as their optical and ferroelectric properties.

4.3 EXPERIMENTAL PROCEDURE

$\text{Bi}_4\text{Ti}_3\text{O}_{12}$ thin films were deposited in a MOCVD apparatus which is shown in Fig. 4.1. $\text{Bi}(\text{C}_6\text{H}_5)_3$ and $\text{Ti}(\text{C}_2\text{H}_5\text{O})_4$ were used as the precursors. The precursors were kept at desired temperatures within 1°C accuracy and carried by nitrogen gas into the reactor during deposition. Source temperatures in the range of $165\text{--}170^\circ\text{C}$ for $\text{Bi}(\text{C}_6\text{H}_5)_3$ and $75\text{--}120^\circ\text{C}$ for $\text{Ti}(\text{C}_2\text{H}_5\text{O})_4$ were employed to obtain desirable vapor pressures for this study. Pure oxygen was used as a dilute gas. Depositions were carried out at reduced pressures (6 torr). Substrate temperatures were varied from 450 to 500°C . The typical deposition conditions are listed in Table 4.1.

The identification of $\text{Bi}_4\text{Ti}_3\text{O}_{12}$ phases was carried out by an X-ray diffractometer with $\text{CuK}\alpha$ radiation. The composition of the films was investigated using energy dispersive spectroscopy (EDS). Scanning electron microscopy (SEM) was used to study the surface morphology of the films. Film thicknesses, refractive indices (n), and extinction coefficients (k) were obtained from UV-VIS-NIR transmission measurements. For the ferroelectric property measurement, $\text{Bi}_4\text{Ti}_3\text{O}_{12}$ film was deposited on a $\text{Pt}/\text{Ti}/\text{SiO}_2/\text{Si}$ substrate and contacted with $2.14 \times 10^{-4} \text{ cm}^2$ palladium as top electrodes. A Sawyer-Tower circuit at 60 Hz was used to measure the ferroelectric properties.

4.4 RESULTS AND DISCUSSION

For the conditions described in Table 4.1, film growth rates were typically in the range of $3.9\text{--}12.5 \text{ nm/min}$. In the range of experimental parameters

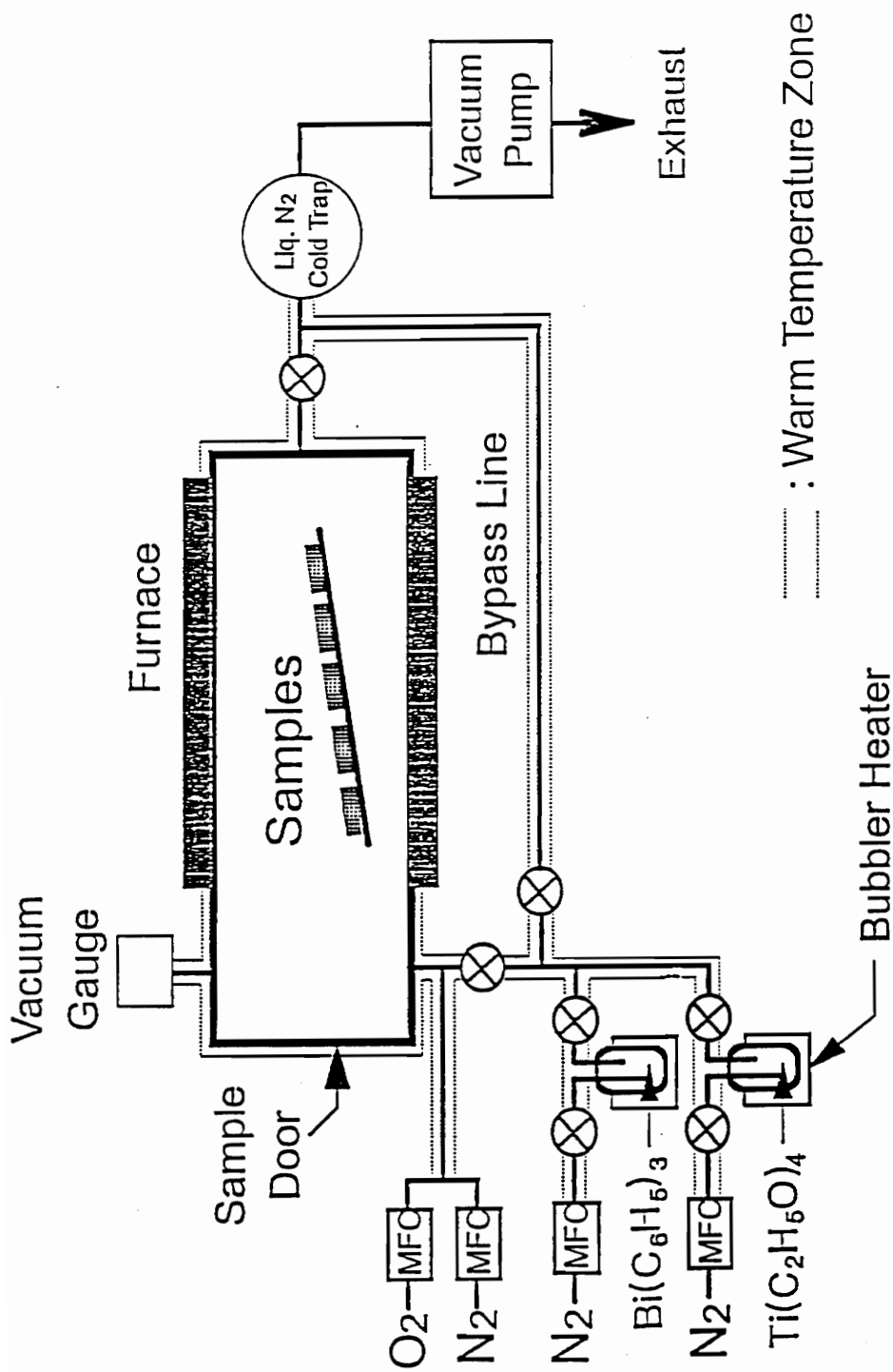


Figure 4.1 Schematic diagram of apparatus for MOCVD Bi₄Ti₃O₁₂ thin films.

Table 4.1 Typical deposition conditions for MOCVD $\text{Bi}_4\text{Ti}_3\text{O}_{12}$ thin films

Precursors	$\text{Bi}(\text{C}_5\text{H}_5)_3$	$\text{Ti}(\text{C}_2\text{H}_5\text{O})_4$
Precursors Temp.($^\circ\text{C}$)	165–170	75–127
Carrier Gas(sccm, N_2)	30–50	0–8
Substrate	Sapphire, Pt/Ti/ SiO_2 /Si, Si	
Substrate Temp.($^\circ\text{C}$)	450–500	
Dilute Gas (sccm, O_2 & N_2)	650	
Total Pressure(torr)	6	

investigated, source temperature, substrate temperature and carrier gas flow rate were found to have significant effect on the film composition. Fig. 4.2 shows the variation of the composition with the source temperature of $\text{Ti}(\text{C}_2\text{H}_5\text{O})_4$ and carrier gas flow rate of $\text{Bi}(\text{C}_6\text{H}_5)_3$, at fixed source temperature of $\text{Bi}(\text{C}_6\text{H}_5)_3$ and no carrier gas for $\text{Ti}(\text{C}_2\text{H}_5\text{O})_4$. The Bi/Ti ratio increased with the increasing carrier gas flow rate and the decreasing source temperature. The variation of Bi/Ti ratio with substrate temperature was also studied. It was found that Bi/Ti ratio dropped considerably at a substrate temperature of 450°C , as shown in Fig. 4.3. In this study, the stoichiometry of the films were mainly controlled by varying the individual precursor temperature and the carrier gas flow rate, and the desired Bi/Ti ratio was achieved by optimizing the processing parameters.

Both as-deposited and annealed MOCVD $\text{Bi}_4\text{Ti}_4\text{O}_{12}$ films were specular, crack-free, uniform, adhered well on Si, sapphire and Pt/Ti/SiO₂/Si substrates and were highly transparent on sapphire substrate. The surface morphologies of the annealed films were investigated by SEM, and were shown in Fig. 4.4. The SEM micrographs showed that the films were dense and smooth on all substrates. The grains were very fine and uniformly distributed. The average grain size was estimated to be around $0.1\ \mu\text{m}$.

The stoichiometric MOCVD $\text{Bi}_4\text{Ti}_3\text{O}_{12}$ thin film prepared on Si substrate was used for structure study. Fig. 4.5 displays the X-ray diffraction (XRD) patterns for the $\text{Bi}_4\text{Ti}_3\text{O}_{12}$ film at different post-deposition annealing temperatures. $\text{Bi}_4\text{Ti}_3\text{O}_{12}$ phase was observed in the as-deposited thin film. Crystallinity was improved as the annealing temperature was increased. The XRD patterns also revealed that

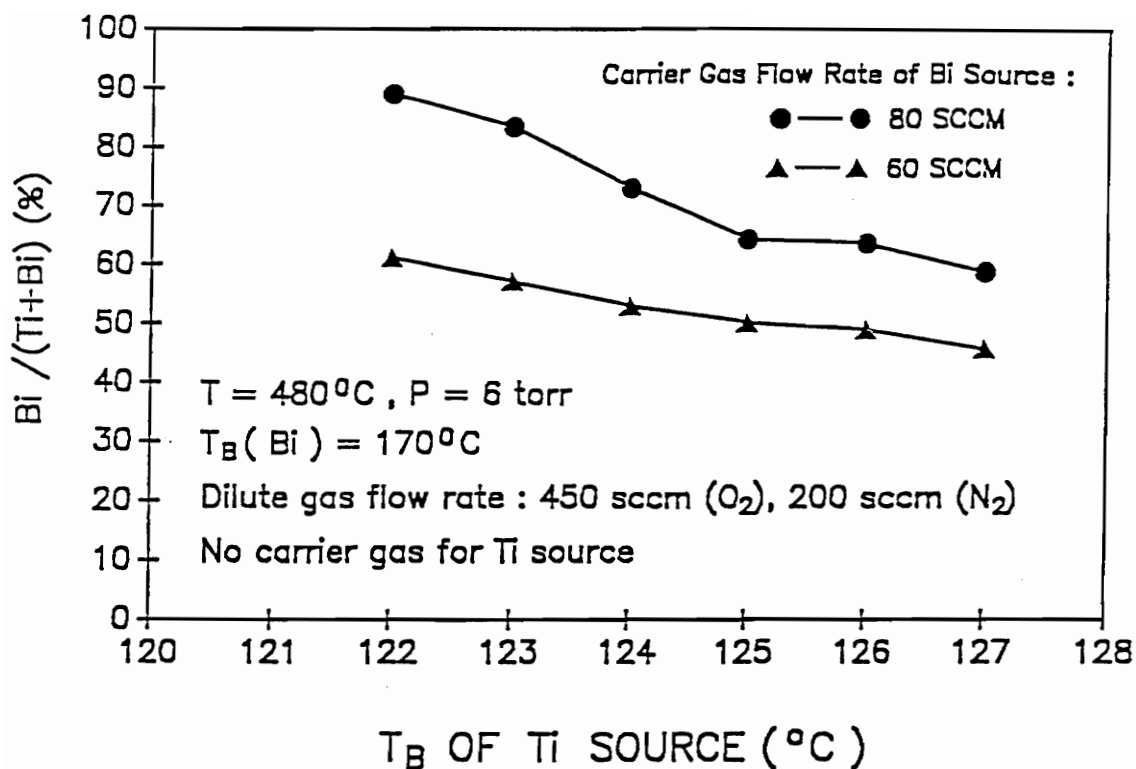


Figure 4.2 Variation of thin film composition with source temperature and carrier gas flow rate.

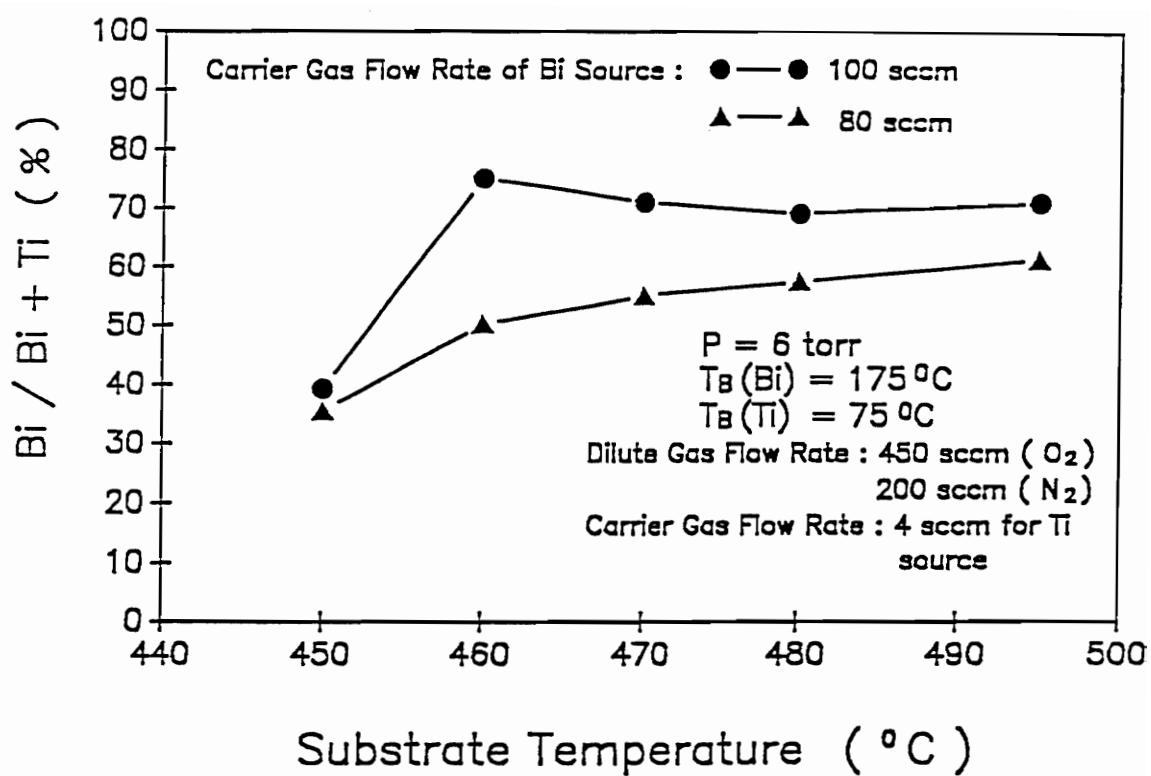


Figure 4.3 Variation of thin film composition with substrate temperature.

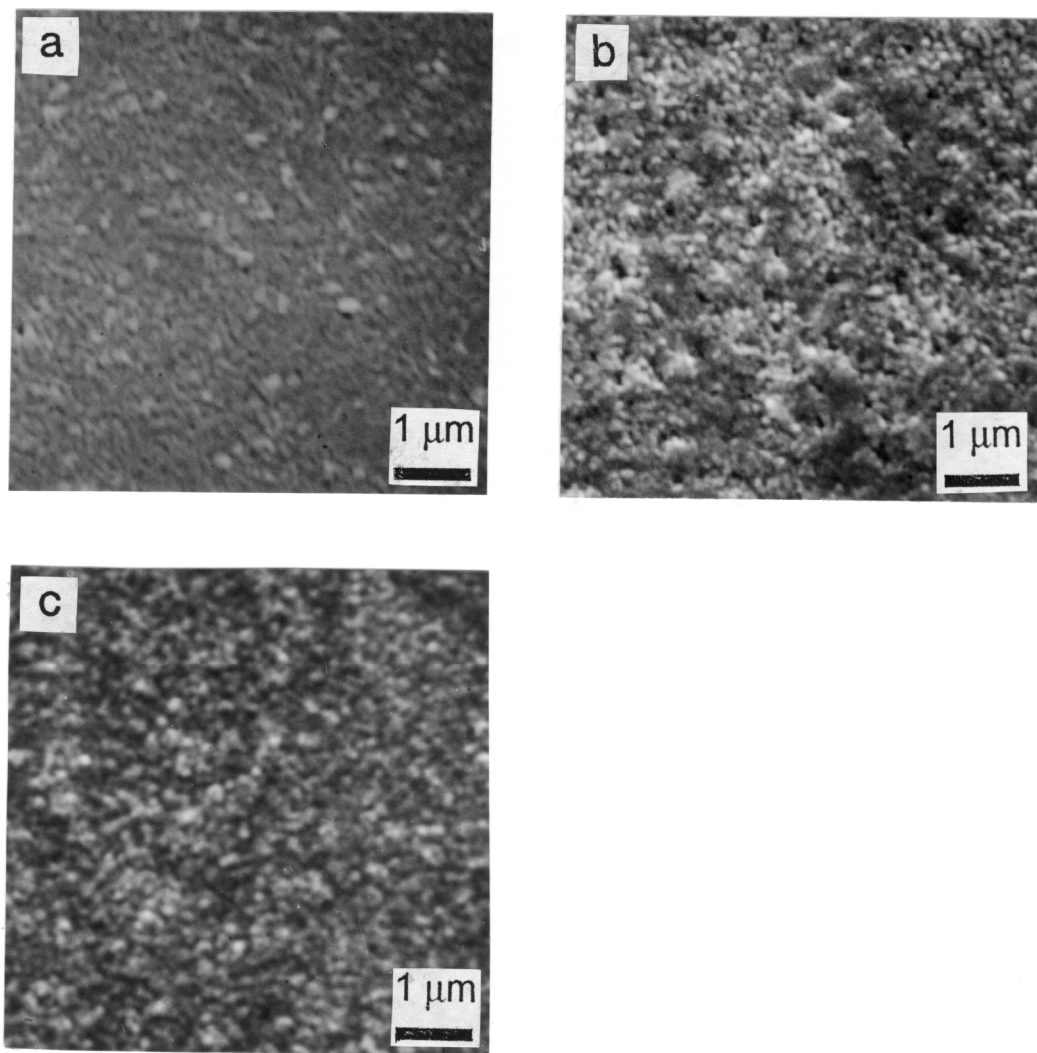


Figure 4.4 SEM micrographs of MOCVD $\text{Bi}_4\text{Ti}_3\text{O}_{12}$ thin film annealed at 550°C : (a) on Si, (b) on Pt/Ti/ SiO_2 /Si, (c) on sapphire substrates.

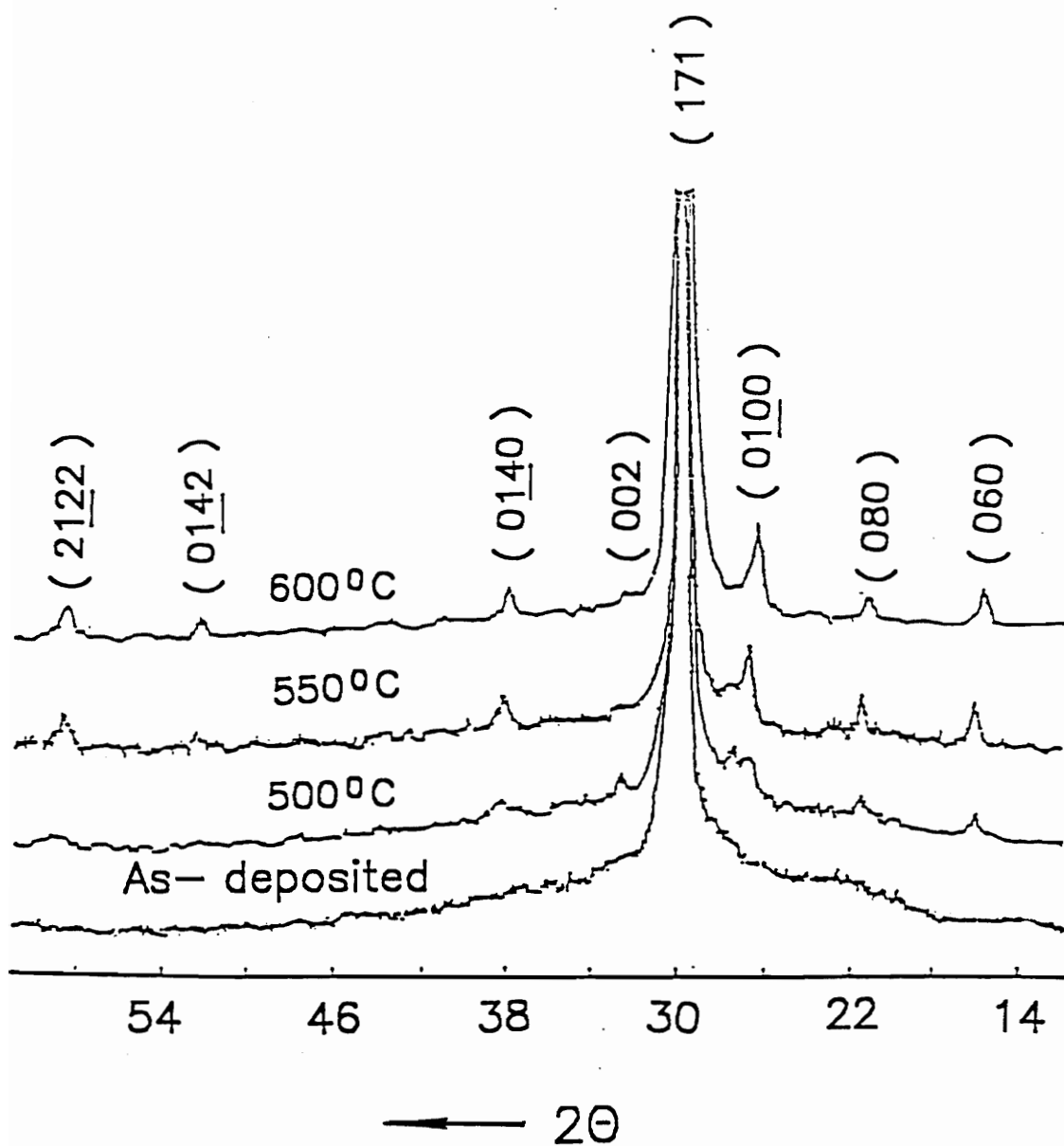


Figure 4.5 X-ray diffraction patterns of the $\text{Bi}_4\text{Ti}_3\text{O}_{12}$ Film at different post-deposition annealing temperature.

good crystalline films were obtained with no secondary phases and no preferred orientation, even at annealing temperatures as low as 550°C.

The AES depth profile of the annealed MOCVD $\text{Bi}_4\text{Ti}_3\text{O}_{12}$ film on Pt/Ti/SiO₂/Si is shown in Fig. 4.6. The composition of the film was uniform except the Bi content decreased and the Ti content increased at the film/substrate interface.

Figure 4.7 shows the typical D-E hysteresis loop of the MOCVD $\text{Bi}_3\text{Ti}_4\text{O}_{12}$ film on Pt/Ti/SiO₂/Si substrate. The film was annealed at 550°C for one hour to obtain good crystallinity. The Bi/Ti ratio of the film was 57/43 by EDS measurement. The spontaneous polarization P_s , remnant polarization P_r , and coercive field E_c had values of 26.5 $\mu\text{C}/\text{cm}^2$ and 19.6 $\mu\text{C}/\text{cm}^2$, 244.3 kV/cm, respectively.

The UV-VIS-NIR transmission and reflectance spectra of the MOCVD $\text{Bi}_4\text{Ti}_3\text{O}_{12}$ film on the sapphire substrate is shown in Fig. 4.8. The transmission spectrum illustrates that the transmittance drops to 0% (the absorption edge) at $\lambda = 338$ nm and has a value of 64% at $\lambda = 2000$ nm. An envelope method was used to calculate the film thickness as well as the refractive index, and extinction coefficient of the film as a function of wavelength. The film thickness calculated using this method is 752 nm. The n and k values were 2.507 and 2.88×10^{-3} , respectively, at $\lambda=633$ nm. The high refractive index value, compared to the value of 2.33 from sol-gel films [7], indicates the $\text{Bi}_4\text{Ti}_3\text{O}_{12}$ film is dense. The very low extinction coefficient illustrates the nature of the specular and highly transparent

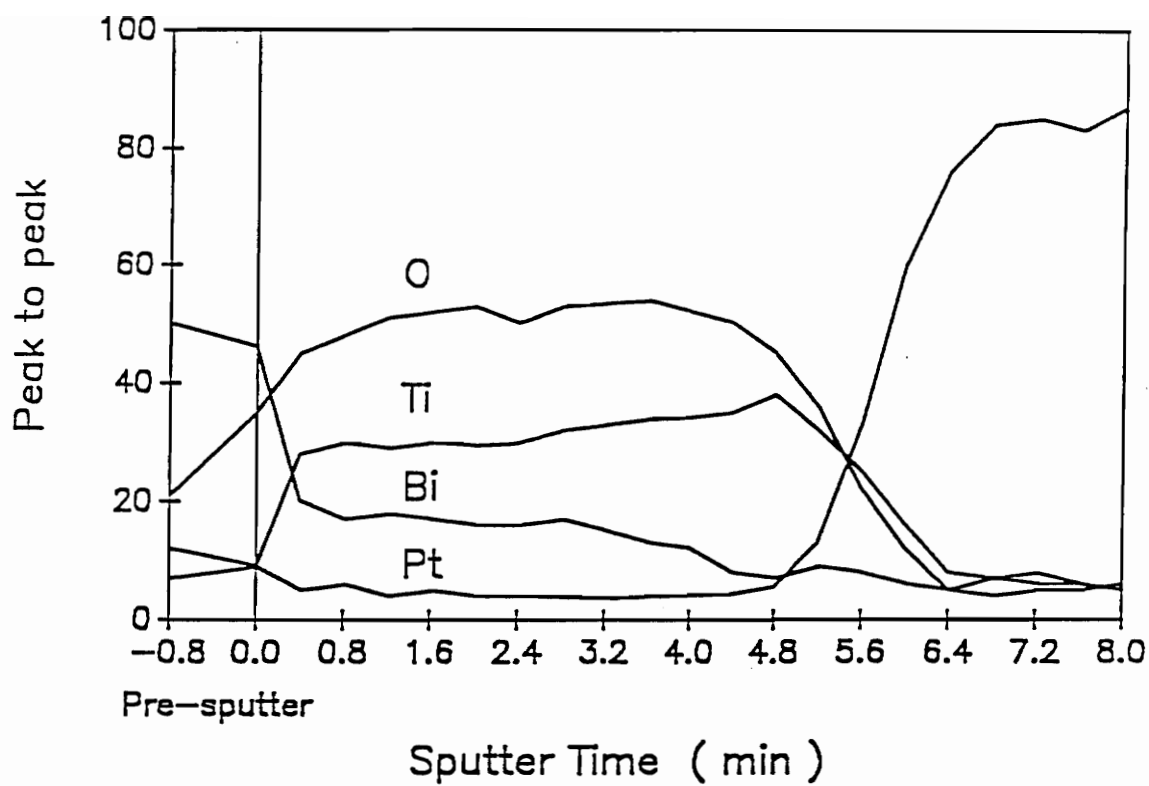


Figure 4.6 AES depth profile of 550°C annealed MOCVD Bi₄Ti₃O₁₂ film.

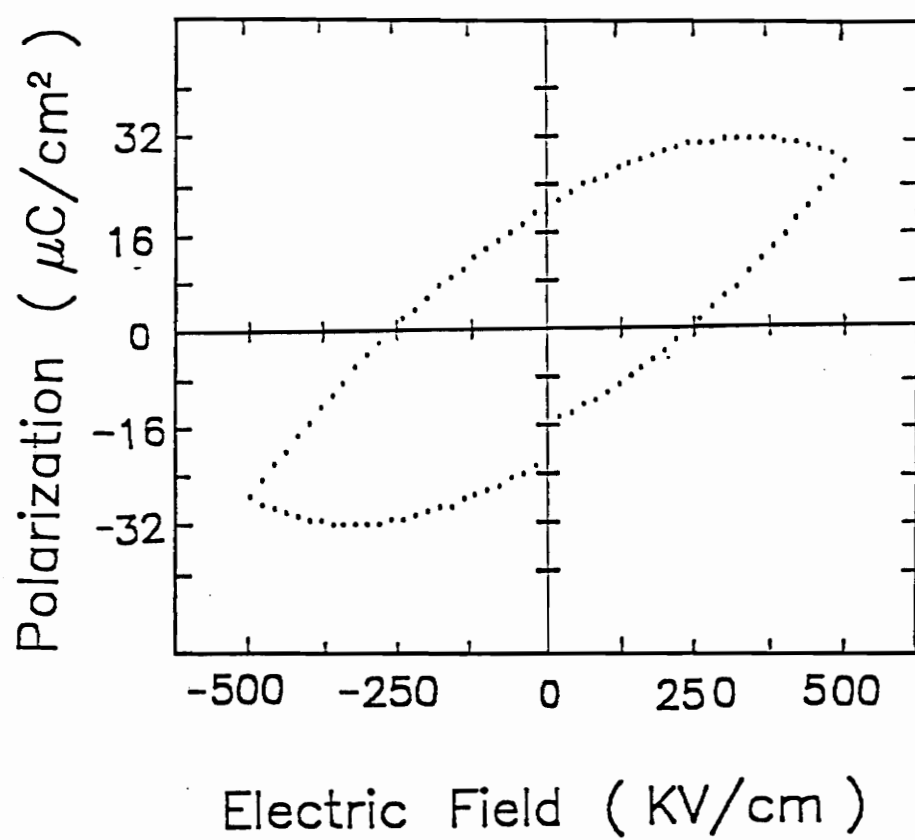


Figure 4.7 Typical D–E hysteresis loop of MOCVD $\text{Bi}_4\text{Ti}_3\text{O}_{12}$ film.

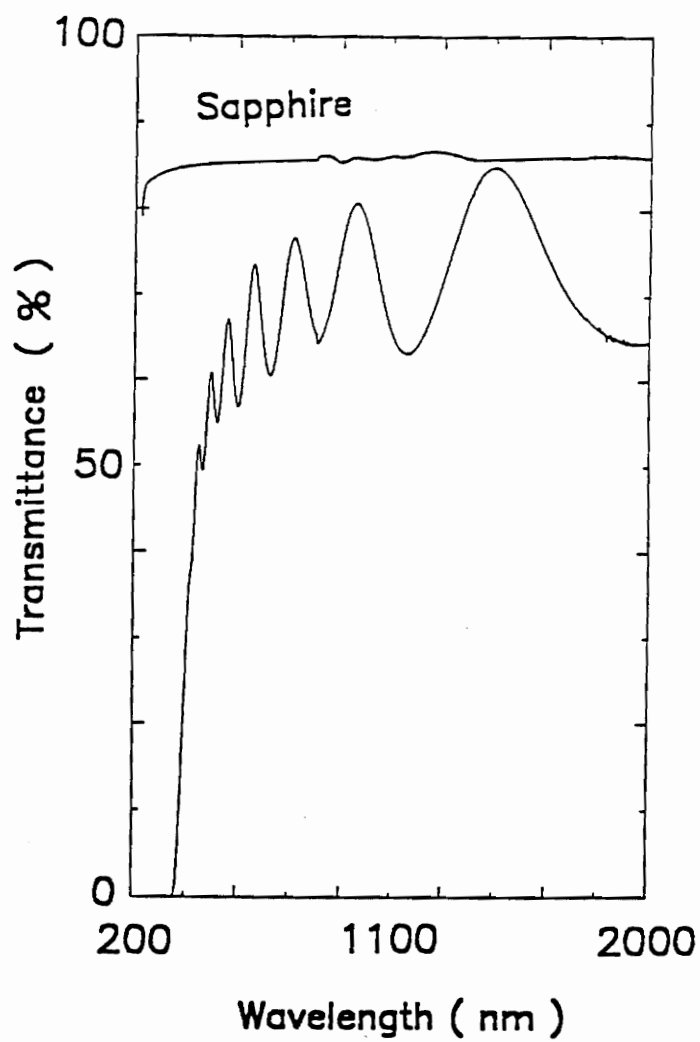


Figure 4.8 Optical transmission and reflection spectrum of MOCVD $\text{Bi}_4\text{Ti}_3\text{O}_{12}$ film on sapphire substrate.

film. The n and k as a function of wavelength are shown in Fig. 4.9.

4.5 SUMMARY

Crystalline $\text{Bi}_4\text{Ti}_3\text{O}_{12}$ thin films were successfully and reproducibly fabricated at low temperature (470°C) on Si, sapphire, and Pt/Ti/ SiO_2 /Si substrates by an optimized MOCVD process. The Bi/Ti ratios of the films were controlled by varying the MOCVD parameters, namely precursor temperature, carrier gas flow rate, and deposition temperature. The ESCA spectrum showed no carbon contamination in the bulk of the film. A high refractive index (2.507) was obtained at $\lambda = 633$ nm in the 550°C annealed film. Very fine grains were observed for the films on all three different substrates used. The D–E hysteresis loop was observed with the ferroelectric properties of $P_s = 26.5 \mu\text{C}/\text{cm}^2$, $P_r = 19.6 \mu\text{C}/\text{cm}^2$, and $E_c = 244.3 \text{ kV}/\text{cm}$.

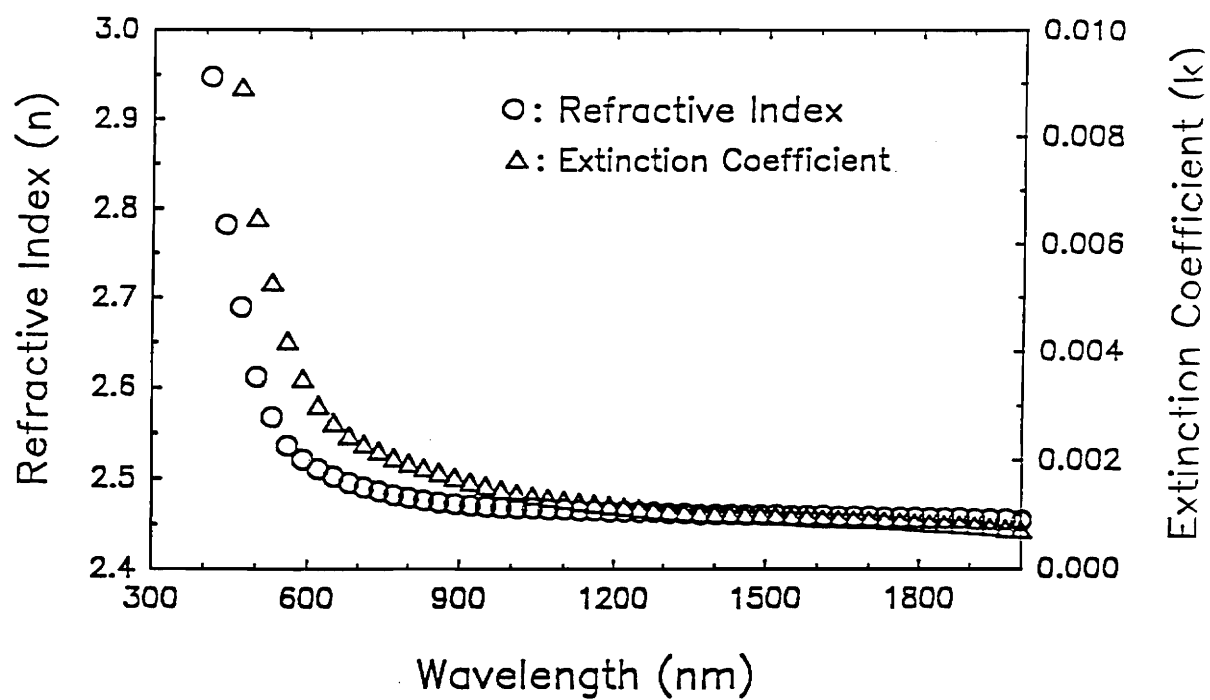


Figure 4.9 Variation of refractive index and extinction coefficient of MOCVD $\text{Bi}_4\text{Ti}_3\text{O}_{12}$ film with wavelength.

ACKNOWLEDGMENTS

We wish to acknowledge the support of DARPA through a project from ONR to this study. This work was also partially supported by Center for Advanced Ceramic Materials, the Virginia Center for Innovative Technology.

4.6 REFERENCES

1. R. Ramesh, K. Luther, B. Wilkens, D. L. Hart, E. Wang, and J. M. Tarascon, "Epitaxial Growth of Ferroelectric Bismuth Tetanate Thin Films by Pulsed Laser Deposition," *Appl. Phys. Lett.*, 57 1505 (1990).
2. S. Y. Wu, W. J. Takei, and M. H. Francombe, "Electro-optic Contrast Observations in Single-Domain Epitaxial Films of Bismuth Tetanate," *Appl. Phys. Lett.*, 22, 26 (1973).
3. K. Sugibuchi, Y. Kurogi, and N. Endo, "Ferroelectric Field-effect Memory Device Using $\text{Bi}_4\text{Ti}_3\text{O}_{12}$ Film," *J. Appl. Phys.*, 46, 2877 (1975).
4. R. Ramesh, A. Inam, W. K. Chan, B. Wilkens, K. Myers, K. Temschnig, D. L. Hart, and J. M. Tarascon, "Epitaxial Cuprate Superconductor/Ferroelectric Heterostructures," *Science*, 252, 944 (1991).
5. N. Maffei and S. B. Krupanidhi, "Excimer Laser-ablated Bismuth Titanate Thin Films," *Appl. Phys. Lett.*, 60, 781 (1992).
6. H. Buhay, S. Singaroy, W. H. Kasne, and M. H. francombe, "Pulsed Laser Deposition and Ferroelectric Characterization of Bismuth Titanate Films," *Appl. Phys. Lett.*, 58, 1470 (1991).
7. P. C. Joshi and Abhai Mansingh, "Structural and Optica Properties of

Ferroelectric $\text{Bi}_4\text{Ti}_3\text{O}_{12}$ Thin Films by Sol-gel Technique," Appl. Phys. lett., 59, 2389 (1991).

8. M. Miyajima, R. Muhannet and M. Okada, "Preparation and Electric Properties of Ferroelectric $\text{Bi}_4\text{Ti}_3\text{O}_{12}$ Thin Films by MOCVD," J. Chem. Soci. of Jpn., 10, 1378 (1991).

CHAPTER 5 SUMMARY

Pure and conducting RuO_2 thin films were successfully fabricated at a low temperature (550°C) on Si, SiO_2/Si and quartz substrates by MOCVD technique. The process parameters were optimized. Lower deposition rate and sufficient oxygen pressure favored the formation of RuO_2 phase. Furthermore, film structures were not only dependent on MOCVD process parameters but also on substrate material. The as-deposited films were crack-free and adhered well on the substrates. The Auger electron spectroscopy depth profile showed a good compositional uniformity across the bulk of the films. The MOCVD RuO_2 thin films exhibited a resistivity as low as $60\ \mu\Omega/\text{cm}$. In addition, reflectance of RuO_2 in the UV–VIS–NIR region showed a metallic character.

$\text{Zr}(\text{thd})_4$ was synthesized and the process was optimized. Because $\text{Zr}(\text{thd})_4$ is thermal stable and has acceptable vapor pressure, It has been proved to be a very good precursor for depositing excellent quality MOCVD ZrO_2 thin films. The as-deposited ZrO_2 thin films were fine-grained and stoichiometric. In addition, the deposition rate can be easily controlled from 6 to 18 nm/min by adjusting the deposition parameters in the range of experimental parameters investigated. Only the tetragonal phase was observed in the as-deposited films. The tetragonal phase transformed progressively into the monoclinic phase as the films were subjected to

high-temperature annealing. The FTIR spectra of both the tetragonal and monoclinic ZrO_2 thin film were obtained. The optical properties of the ZrO_2 thin films as a function of wavelength, in the range of 200 nm to 2000 nm, were investigated. In addition, a simplified theoretical model which considers only a surface reaction was used to analyze the deposition of ZrO_2 film. The deposition rates can be predicted well for various deposition conditions in the hot wall reactor.

Crystalline $\text{Bi}_4\text{Ti}_3\text{O}_{12}$ thin films were successfully and reproducibly fabricated at low temperature (470°C) on Si, sapphire, and Pt/Ti/ SiO_2 /Si substrates by an optimized MOCVD process. The Bi/Ti ratios of the films were controlled by varying the MOCVD parameters, namely precursor temperature, carrier gas flow rate, and deposition temperature. The ESCA spectrum showed no carbon contamination in the bulk of the film. A high refractive index (2.507) was obtained at $\lambda = 633$ nm in the 550°C annealed film. Very fine grains were observed for the films on all three different substrates used. The D-E hysteresis loop was observed with the ferroelectric properties of $P_s = 26.5 \mu\text{C}/\text{cm}^2$, $P_r = 19.6 \mu\text{C}/\text{cm}^2$, and $E_c = 244.3 \text{ kV}/\text{cm}$.

VITA

Jie Si was born on August 25, 1963 in Shanghai, China. She entered Shanghai Jiao Tong University(SJTU) in 1981. She received her Bachelor of Science from SJTU in Materials Science and Engineering in 1985. Her interest in electronic thin film materials led her to further study in The Information Storage Research Center, SJTU where she earned her Master of Science in Electrical Engineering. She began her graduate studies at Virginia Polytechnic Institute and State University in Spring 1991.

After graduation, she will continue to work in materials science research area.